

A 38 Million Year Old Mini-Neptune in the Kepler Field

L. G. BOUMA,^{1,2,*} J. L. CURTIS,^{3,4} K. MASUDA,⁵ L. A. HILLENBRAND,² G. STEFANSSON,^{1,†} H. ISAACSON,⁶
N. NARITA,^{7,8,9,10} A. FUKUI,^{7,10} M. IKOMA,¹¹ M. TAMURA,^{12,9,13} A. L. KRAUS,¹⁴ E. FURLAN,¹⁵
C. L. GNILKA,¹⁶ K. V. LESTER,¹⁶ AND S. B. HOWELL¹⁶

¹*Department of Astrophysical Sciences, Princeton University, 4 Ivy Lane, Princeton, NJ 08540, USA*

²*Cahill Center for Astrophysics, California Institute of Technology, Pasadena, CA 91125, USA*

³*Department of Astronomy, Columbia University, 550 West 120th Street, New York, NY 10027, USA*

⁴*Department of Astrophysics, American Museum of Natural History, New York, NY 10024, USA*

⁵*Department of Earth and Space Science, Osaka University, Osaka 560-0043, Japan*

⁶*Astronomy Department, University of California, Berkeley, CA 94720, USA*

⁷*Komaba Institute for Science, The University of Tokyo, Tokyo 153-8902, Japan*

⁸*Japan Science and Technology Agency, PRESTO, Tokyo 153-8902, Japan*

⁹*Astrobiology Center, Tokyo 181-8588, Japan*

¹⁰*Instituto de Astrofísica de Canarias (IAC), 38205 La Laguna, Tenerife, Spain*

¹¹*Division of Science, National Astronomical Observatory of Japan, Tokyo 181-8588, Japan*

¹²*Department of Astronomy, University of Tokyo, Tokyo 113-0033, Japan*

¹³*National Astronomical Observatory of Japan, Tokyo 181-8588, Japan*

¹⁴*Department of Astronomy, The University of Texas at Austin, Austin, TX 78712, USA*

¹⁵*NASA Exoplanet Science Institute, Caltech/IPAC, Pasadena, CA 91125, USA*

¹⁶*NASA Ames Research Center, Moffett Field, CA 94035, USA*

(Received —; Revised —; Accepted —)

Submitted to AAS Journals

ABSTRACT

Kepler 1627A is a G8V star previously known to host a $3.3R_{\oplus}$ mini-Neptune on a 7.2 day orbit. The star was observed by the Kepler space telescope because it is nearby ($d = 329 \pm 3$ pc) and it resembles the Sun. Here we show using Gaia kinematics, TESS stellar rotation periods, and spectroscopic lithium abundances that Kepler 1627 is a member of the 38^{+6}_{-5} Myr old δ Lyr cluster. To our knowledge, Kepler 1627Ab is the youngest planet with a precise age yet found by the main Kepler mission. The Kepler data show two notable anomalies. First, after removal of the stellar variability, the average Kepler transit profile appears to be asymmetric. One possible explanation is that a dusty atmospheric outflow is present, but this remains to be confirmed. Second, the individual transits show a correlation between the transit time and the local slope of the light curve. Interpreted in a framework in which unresolved starspot-crossing events cause the transit timing variations, this suggests that the planet is on a prograde orbit. We present Keck/HIRES observations that are consistent with the latter point, though the data do not have the precision necessary to claim a detection of the spectroscopic transit. More broadly, the δ Lyr cluster is one of many stellar groups whose properties have been clarified using Gaia; many other exoplanet hosts belong to these new clusters. Verifying the results of Gaia clustering analyses using TESS rotation periods offers a promising path toward expanding the census of age-dated planets, and our corresponding understanding of planetary evolution.

Keywords: exoplanet evolution (491), open star clusters (1160), stellar ages (1581)

Corresponding author: L. G. Bouma

luke@astro.caltech.edu

* 51 Pegasi b Fellow

† Henry Norris Russell Fellow

1. INTRODUCTION

While thousands of exoplanets have been discovered orbiting nearby stars, the vast majority of them are several billion years old. This makes it difficult to test origin theories for the different families of planets, since many evolutionary processes are expected to operate on timescales of less than 100 million years.

For instance, the “mini-Neptunes”, thought to be made of molten rocky cores (Kite et al. 2020) and extended atmospheric envelopes of hydrogen and helium, are expected to shrink in size by factors of several over their first 10^8 years. Specifically, in the models of Owen & Wu (2016) and Owen (2020), the $\approx 5 M_\oplus$ planets start with sizes of $4\text{--}12 R_\oplus$ shortly after the time of disk dispersal ($\lesssim 10^7$ years), and shrink to sizes of $2\text{--}4 R_\oplus$ by 10^8 years. While the majority of this change is expected to occur within the first few million years after disk dispersal (Owen & Wu 2016), the combination of stellar irradiation and internal heat may also power a more gradual outflow which can eventually deplete or entirely strip the envelope from the rocky core (Owen & Wu 2013; Ginzburg et al. 2018). Discovering young planets, measuring their masses, and detecting their atmospheric outflows are key steps toward testing this paradigm, which is often invoked to explain the observed radius distribution of mature exoplanets (Fulton et al. 2017).

The K2 and TESS missions have now enabled the detection of about ten close-in planets younger than 100 million years, all smaller than Jupiter (Mann et al. 2016; David et al. 2016, 2019; Newton et al. 2019; Bouma et al. 2020; Plavchan et al. 2020; Rizzuto et al. 2020; Martioli et al. 2021). The Kepler mission however has not yielded any planets with precise ages below one gigayear (Meibom et al. 2013). The reason is that during the main Kepler mission (2009–2013), only four open clusters were known in the Kepler field, with ages spanning 0.7 Gyr to 9 Gyr (Meibom et al. 2011). Though isochronal, gyrochronal, and lithium-based analyses suggest that younger Kepler planets do exist (Berger et al. 2018; David et al. 2021), accurate and precise age measurements typically require an ensemble of stars. Fortunately, recent analyses of the Gaia data have since expanded our knowledge of cluster memberships (e.g., Cantat-Gaudin et al. 2018; Zari et al. 2018; Kounkel & Covey 2019; Meingast et al. 2021; Kerr et al. 2021). As part of our Cluster Difference Imaging Photometric Survey (CDIPS, Bouma et al. 2019), we concatenated the available analyses from the literature, which yielded a list of candidate young and age-dated stars (see Appendix A).

Matching our young star list against stars observed by Kepler yielded two discoveries. The first, to be discussed in an upcoming analysis by J. Curtis et al., is that Kepler observed the ≈ 350 Myr open cluster Theia 520 (UBC 1). At least six Kepler planets are known in the cluster from the Kepler-52 and Kepler-968 systems (Rowe et al. 2014; Jontof-Hutter et al. 2021). The second discovery, and the focus of this work, is that Kepler observed a portion of the δ Lyr cluster (Stephenson-1; Theia 73; Stephenson 1959). Figure 1 shows the overlap between the Kepler field and the cluster.

A previous clustering analysis of the Gaia data reported that Kepler 1627 (KIC 6184894; KOI 5245; TIC 120105470) is a member of the δ Lyr cluster (Kounkel & Covey 2019). Given the previous statistical validation of the close-in mini-Neptune Kepler 1627b (Tenenbaum et al. 2012; Morton et al. 2016; Thompson et al. 2018), we examined the age of the star and its putative host cluster more closely (Section 2). We find that the δ Lyr cluster is 38^{+6}_{-5} Myr old, and that Kepler 1627 is indeed a member of the cluster. Focusing on the planet itself, we confirm that despite the presence of a previously unreported binary companion, hereafter Kepler 1627B, the planet orbits the G-dwarf primary on an orbit that is likely prograde (Section 3). We conclude by highlighting broader implications for our ability to age-date a statistical sample of planets (Section 4).

2. THE CLUSTER

To assess the age of the cluster and our star of interest, we used a combination of isochronal, gyrochronal, and lithium-based age-dating.

2.1. Color-Absolute Magnitude Diagram

We measured the isochrone age through an empirical approach. The left panel of Figure 2 shows the color-absolute magnitude diagram (CAMD) of stars in the δ Lyr cluster, IC 2602, the Pleiades, and the field. The candidate δ Lyr cluster members shown are selected based on their positions and kinematics (see Appendix B). Those from the Pleiades and IC 2602 are adopted from Cantat-Gaudin et al. (2018), and the field stars are from the Gaia EDR3 Catalog of Nearby Stars (Gaia Collaboration et al. 2021b). We cleaned these following the data filtering criteria discussed in Appendix B of Gaia Collaboration et al. (2018a), except that we weakened the parallax precision requirement to $\varpi/\sigma_\varpi > 5$. These filters were designed to include genuine binaries while omitting instrumental artifacts. We then corrected for extinction by querying the 3-dimensional maps of Capitanio et al. (2017)

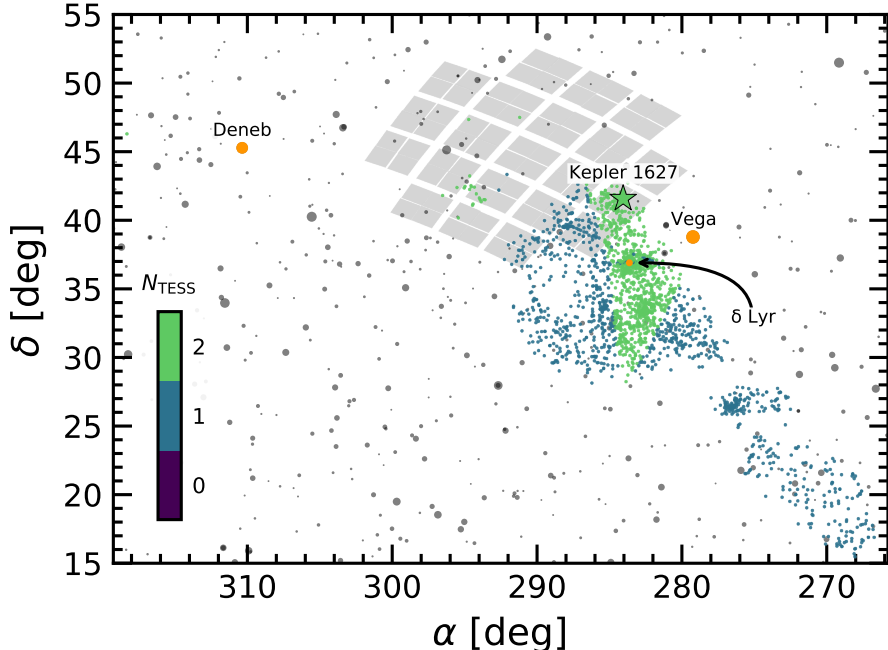


Figure 1. Kepler and TESS views of the δ Lyr cluster. Colored points are kinematically selected candidate δ Lyr cluster members. Both Kepler (gray panels) and TESS observed portions of the cluster. Stars visible by eye ($m_V < 6.5$) are shown in gray; Deneb, Vega, and δ Lyr are orange. Kepler 1627 (green star) was observed during the entirety of the Kepler mission, and to date has been observed for two lunar months by TESS.

and [Lallement et al. \(2018\)](#)¹, and then applied the extinction coefficients $k_X \equiv A_X/A_0$ computed by [Gaia Collaboration et al. \(2018a\)](#) and assumed that $A_0 = 3.1E(B-V)$. For IC 2602, the Pleiades, and the δ Lyr cluster, this procedure yielded a respective mean and standard deviation for the reddening of $E(B-V) = \{0.020 \pm 0.003, 0.045 \pm 0.008, 0.032 \pm 0.006\}$. These values agree reasonably well with previously reported values from the literature (e.g., [Gaia Collaboration et al. 2018a](#); [Kounkel & Covey 2019](#); [Bossini et al. 2019](#)).

Figure 2 shows that the δ Lyr cluster and IC 2602 overlap, and therefore are approximately the same age. In our exploration, we also compared against μ -Tau (62 ± 7 Myr; [Gagné et al. 2020](#)) and the Upper-Centaurus-Lupus (UCL) component of the Sco OB2 association (≈ 16 Myr; [Pecaut & Mamajek 2016](#)). The pre-main-sequence M dwarfs of the δ Lyr cluster were intermediate between the latter two clusters. To turn this heuristic interpolation into an age measurement, we used the empirical method developed by [Gagné et al. \(2020\)](#). In brief, we fitted the pre-main-sequence loci of a set of reference clusters, and the locus of the target δ Lyr cluster was then modeled as a piecewise linear combination of these reference clusters. For our reference clusters, we adopted mem-

bers of UCL, IC 2602, and the Pleiades from [Damineli et al. \(2019\)](#) and [Cantat-Gaudin et al. \(2018\)](#) respectively. We removed binaries by requiring $\text{RUWE} < 1.3$, $\text{radial_velocity_error}$ below the 80th percentile of each cluster’s distribution, and manually excluded stars that were obvious photometric binaries in the CAMD. We then passed a moving box average and standard deviation across the CAMD in 0.10 mag bins, fitted a univariate spline to the binned values, and assembled a piecewise grid of hybrid isochrones spanning the ages between UCL to the Pleiades using Equations 6 and 7 from [Gagné et al. \(2020\)](#).

The ages returned by this procedure depend on the ages assumed for each reference cluster. We adopted a 115 Myr age for the Pleiades, and a 16 Myr age for UCL ([Dahm 2015](#); [Pecaut & Mamajek 2016](#)). The age of IC 2602 however is the most important ingredient, since it receives the most weight in the interpolation. Plausible ages for IC 2602 span 30 Myr to 46 Myr, with slightly older ages being preferred by the lithium-depletion-boundary (LDB) measurements and younger ages by the main-sequence turn-off ([Stauffer et al. 1997](#); [Dobbie et al. 2010](#); [David & Hillenbrand 2015](#); [Randich et al. 2018](#); [Bossini et al. 2019](#); [Bouma et al. 2020](#)). If we were to adopt the 30 Myr age for IC 2602, then the δ Lyr cluster would be 31^{+5}_{-4} Myr old. For the converse extreme of 46 Myr, the δ Lyr cluster would be 44^{+8}_{-7} Myr old. We adopt an inter-

¹ <https://stilism.obspm.fr/>

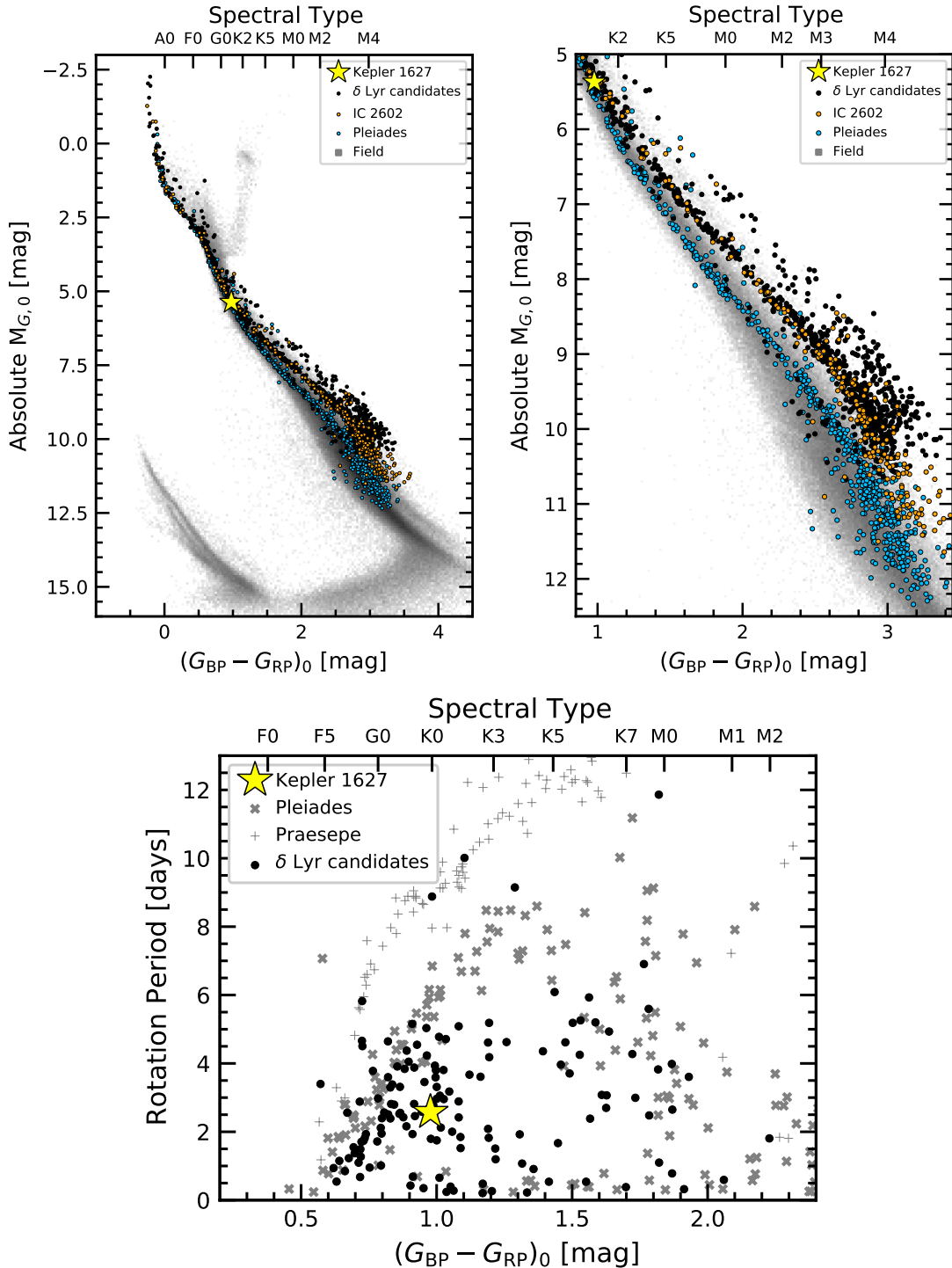


Figure 2. The δ Lyr cluster is 38^{+6}_{-5} Myr old. *Top:* Color-absolute magnitude diagram of candidate δ Lyr cluster members, in addition to stars in IC 2602 (≈ 38 Myr), the Pleiades (≈ 115 Myr; Dahm 2015), and the Gaia EDR3 Catalog of Nearby Stars (gray background). The zoomed right panel highlights the pre-main-sequence. The δ Lyr cluster and IC 2602 are approximately the same isochronal age. *Bottom:* TESS and Kepler stellar rotation period versus dereddened Gaia color, with the Pleiades and Praesepe (650 Myr) shown for reference (Rebull et al. 2016; Douglas et al. 2017). Most candidate δ Lyr cluster members are gyrochronally younger than the Pleiades; outliers are probably field interlopers.

mediate 38 Myr age for IC 2602, which yields an age for the δ Lyr cluster of 38^{+6}_{-5} Myr.² While detailed analyses of the LDB or main-sequence turn-off in the δ Lyr cluster could help resolve the tension between the LDB and isochrone ages, these are beyond our scope.

2.2. Stellar Rotation Periods

Of the 3,071 candidate δ Lyr cluster members reported by Kounkel & Covey (2019), 924 stars were amenable to rotation period measurements ($G < 17$ and $(G_{\text{BP}} - G_{\text{RP}})_0 > 0.5$) and had TESS data available.³ We extracted light curves from the TESS images using the nearest pixel to each star, and regressed them against systematics with the causal pixel model implemented in the unpopular package (Hattori et al. 2021). We then measured candidate rotation periods using a Lomb-Scargle periodogram (Lomb 1976; Scargle 1982; Astropy Collaboration et al. 2018). To enable cuts on crowding, we queried the Gaia source catalog for stars within a $21.^{\circ}0$ radius of the target star (1 TESS pixel). We recorded the number of stars within the aperture with greater brightness than the target star, and with brightness within 1.25 and 2.5 TESS magnitudes of the target star.

We cleaned the candidate TESS rotation period measurements through a combination of automated and manual steps. As a matter of scope, we restricted our attention to the 391 stars discussed in Appendix B in the spatial and kinematic proximity of Kepler 1627. To avoid blending, we also only focused on stars for which no companions were known with a brightness exceeding one-tenth of the target star in a $21.^{\circ}0$ radius. There were 192 stars that met these requirements, and that had TESS data available. For plotting purposes we then imposed a selection based on the strength of the signal itself: we required the Lomb Scargle power to exceed 0.2, and the period to be below 15 days.

The lower panel of Figure 2 shows the resulting 145 stars. The majority of these stars fall below the “slow sequence” of the Pleiades, consistent with a gyrochronological age for the δ Lyr cluster below 100 Myr. Approximately 10 stars appear as outliers above the “slow sequence”. Assuming that they are all false positives (*i.e.*, field interlopers), the rotation period detection fraction would be

² Our exploration of the PARSEC and MIST isochrone models over a grid of ages, metallicities, and reddenings, yielded the best agreement for this ≈ 38 Myr age as well, given $[\text{Fe}/\text{H}] = +0.1$ and $A_V = 0.2$ (Bressan et al. 2012; Choi et al. 2016); this preferred CAMD reddening is higher than the Lallement et al. (2018) value by a factor of two.

³ Kepler rotation periods were derived by McQuillan et al. (2014) for 56 stars; in these cases, we adopted the Kepler rotation period.

$135/192 \approx 70\%$. The rotation period distributions of other 30 Myr to 50 Myr clusters (*e.g.*, IC 2602 and IC 2391) are indistinguishable (Douglas et al. 2021). Binarity is known to be an important factor in the density of stars falling underneath the slow sequence (Meibom et al. 2007; Gillen et al. 2020; Bouma et al. 2021). Appendix C discusses this topic, and finds evidence for similar effects to those previously noted in the literature.

2.3. Age of Kepler 1627

To summarize, the age of the δ Lyr cluster based on the empirical pre-main-sequence interpolation method is 38^{+6}_{-5} Myr. This method hinges on the age adopted for IC 2602, since it is the closest reference cluster in the color-absolute magnitude diagram. Gyrochronologically, while most of the FGK dwarfs in the δ Lyr cluster have not yet converged to a slow sequence, their rotation periods are generally consistent with a 38 Myr age. The most precise age for Kepler 1627 and its planet are therefore identical to the cluster, based on the star’s spatial and kinematic association with the cluster, and the assumption that the planet formed shortly after the star.

Beyond the kinematic and rotational lines of evidence for the youth of Kepler 1627, there is a final consistency check: the abundance of Li I as inferred from the 6708 \AA doublet (*e.g.*, Soderblom et al. 2014). We acquired an iodine-free spectrum from Keck/HIRES on the night of 2021 March 26 using the standard setup and reduction techniques of the California Planet Survey (Howard et al. 2010). Following the equivalent width measurement procedure described by Bouma et al. (2021), we find $\text{EW}_{\text{Li}} = 233^{+5}_{-7} \text{ m\AA}$. Given the effective temperature of Kepler 1627 (Table 1), this measurement is in agreement with expectations for a 38 Myr star (*e.g.*, as measured in IC 2602 by Randich et al. 2018). It is also larger than any lithium equivalent widths measured by Berger et al. (2018) in their analysis of 1,301 Kepler-star spectra.

3. THE PLANET

If the Kepler 1627Ab transit signal is created by a genuine planet, then to our knowledge its age would make it the youngest planet yet found by the main Kepler mission.⁴ The light curve and the phase-folded transit are shown in Figure 3. The photometry is dominated by a quasi-periodic starspot signal with a peak-to-peak amplitude that

⁴ The re-purposed K2 mission however has found two younger systems containing five planets: K2-33b (9 ± 1 Myr; Mann et al. 2016; David et al. 2016) and V1298 Tau (23 ± 4 Myr; David et al. 2019).

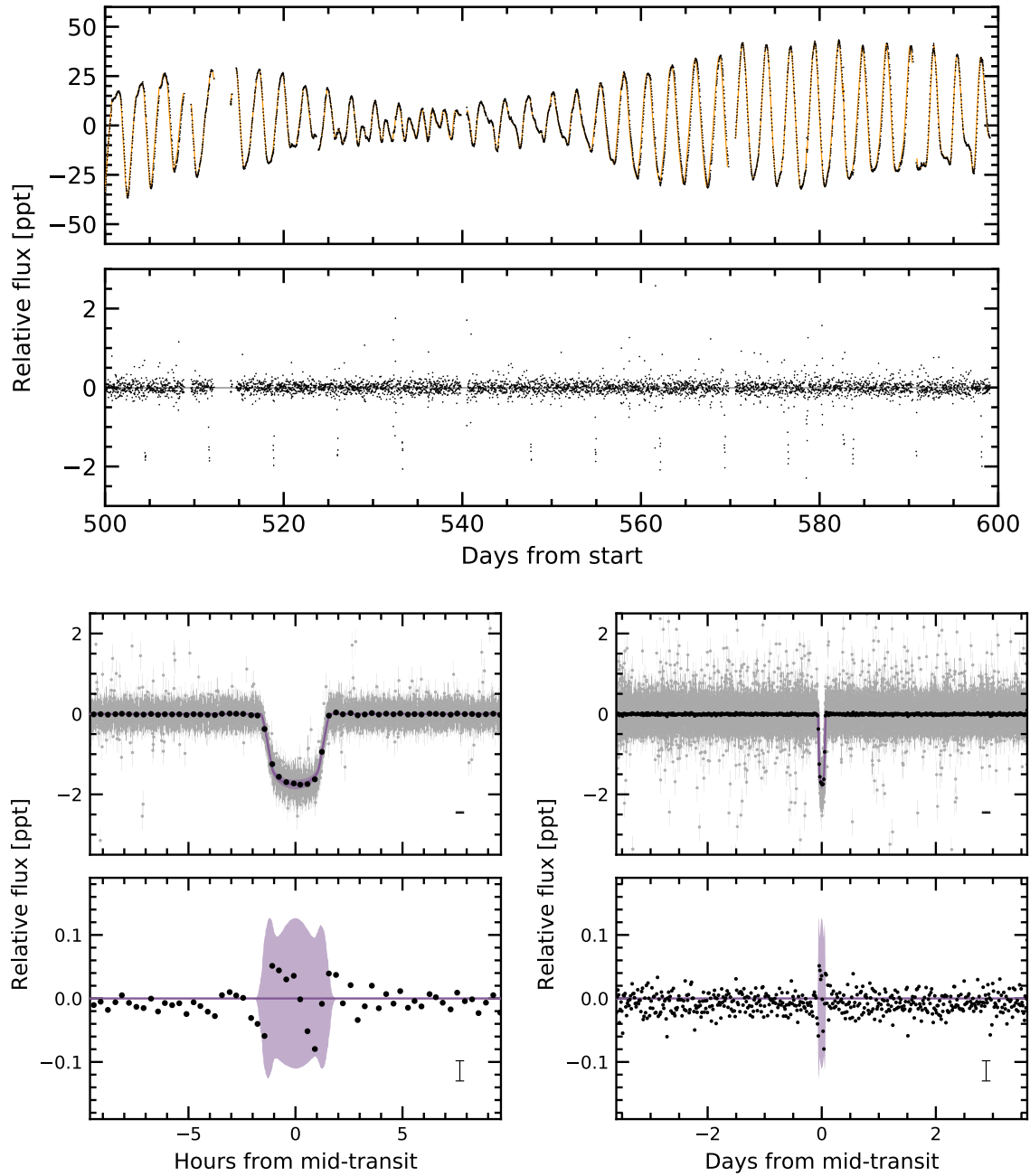


Figure 3. The light curve of Kepler 1627. *Top:* The Kepler data span 1,437 days (3.9 years), sampled at 30 minute cadence; a 100 day segment is shown. The top panel shows the PDCSAP median-subtracted flux in units of parts-per-thousand ($\times 10^{-3}$). The dominant signal is induced by starspots. The stellar variability model (orange line) is subtracted below, revealing the transits of Kepler 1627Ab. The online Figure Set spans the entire 3.9 years of observations. *Bottom:* Phase-folded transit of Kepler 1627Ab with stellar variability removed. Windows over 20 hours (*left*) and the entire orbit (*right*) are shown, and the residual after subtracting the transit is in the bottom-most row. The 2σ model uncertainties and the best-fit model are the light purple band and the dark purple line. Gray points are individual flux measurements; black points bin these to 20 minute intervals, and have a representative 1σ error bar in the lower right of each panel. The asymmetric residual during transit appears to be robust to different detrending methods.

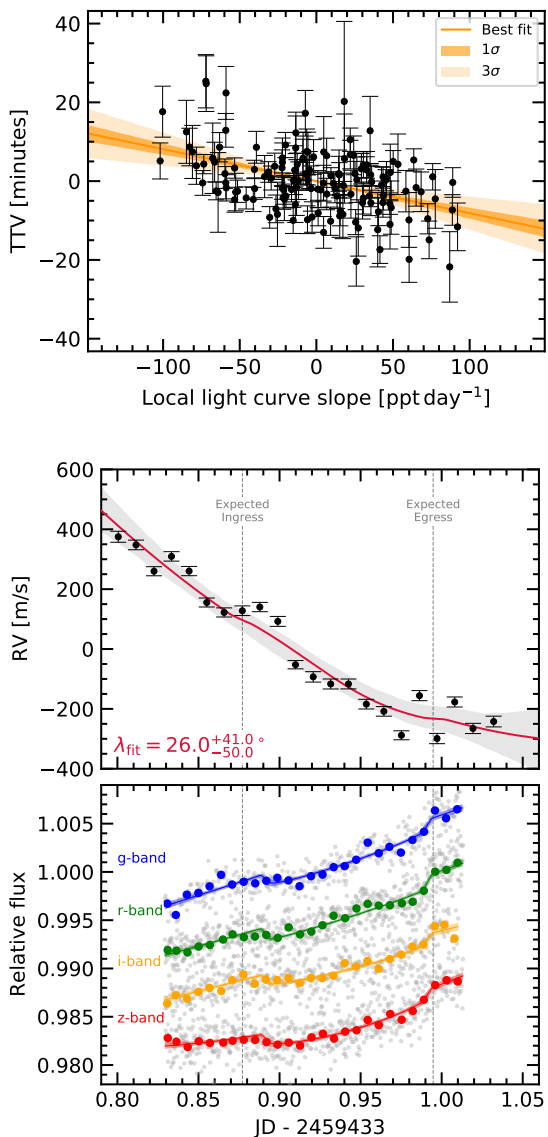


Figure 4. Evidence for a prograde orbit of Kepler 1627 Ab. *Top:* The time of each Kepler transit was measured, along with the local slope of the light curve. The two quantities appear anti-correlated, which is most easily explained by starspot crossings during the first (second) half of transit inducing a positive (negative) TTV, provided that the orbit is prograde (Mazeh et al. 2015). The units along the abscissa are most easily understood by considering that the stellar flux changes by ~ 60 ppt per half rotation period (~ 1.3 days). *Bottom:* Radial velocities acquired using Keck/HIRES during the transit of 2021 Aug 7, observed simultaneously with MuSCAT3. Shaded bands show 2σ model uncertainties. The photometric transit depths are consistent across the *griz* bandpasses. The best-fitting model including the RM effect and a quadratic trend in time is shown with the red line. The radial velocity scatter between exposures prevents a significant detection of the RM effect.

varies between 2% and 8%. The signal repeats every 2.642 ± 0.042 days, where the quoted uncertainty is based on the scatter in rotation periods measured from each individual Kepler quarter. Our model for the starspot signal is discussed in detail in Appendix D, and the adopted stellar parameters are listed in Table 1. The stellar mass, radius, and effective temperature are found by interpolating against a 38 Myr MIST isochrone. Their systematic uncertainties are taken to be the difference between the PARSEC and MIST isochrones, and the reported uncertainties are a quadrature sum of the statistical and systematic components. The transit fitting results, given in Table 2, are broadly consistent with a mini-Neptune sized planet ($3.34 \pm 0.18 R_\oplus$) on a close-in circular⁵ orbit around a G8V star ($0.88 \pm 0.02 R_\odot$).

Could this transit signal be produced by anything other than a planet orbiting this near-solar analog? Morton et al. (2016) validated the planet based on the transit shape, arguing that the most probable false positive scenario was that of a background eclipsing binary, which had a model-dependent probability of $\approx 10^{-5}$. As we describe in Appendix E however, Kepler 1627A is accompanied by a low-mass stellar companion ($M_B \approx 0.33 M_\odot$). We therefore reassessed false positive scenarios in some detail.

There are two new lines of evidence that confirm the planetary interpretation. First, the transit duration and the orbital period are inconsistent with an eclipsing body around the M-dwarf companion: we find $\rho_* = 2.00 \pm 0.24 \text{ g cm}^{-3}$, while the theoretically expected density for the companion is $\approx 4.6 \text{ g cm}^{-3}$ (Table 2; Choi et al. 2016). The transit duration is therefore too long to be explained by a star eclipsing the M dwarf secondary at 10σ .

The second line of confirmatory evidence comes by analyzing the individual Kepler transit times. We isolated each of the 144 observed transits to within ± 4.5 hr of each transit, and fitted each window with both *i*) a local second-order polynomial and transit, and *ii*) a local linear trend. We let the mid-time of each transit float, and then calculated the residual between the measured mid-time and that of a periodic orbit. This residual, the transit timing variation (TTV), is plotted in Figure 4 against the local linear slope. A significant correlation of $-0.0564 \pm 0.0098 \text{ ppt day}^{-1}$ is observed. Fewer than ten Kepler Objects of Interest have shown this correlation (Holczer et al. 2015), which is most readily interpreted as a TTV induced by unresolved starspot crossings (Mazeh et al. 2015). This is only possible if the planet tran-

⁵ Our transit fitting yields $e < 0.48$ at 2σ ; the constraints on the eccentricity are not particularly strong.

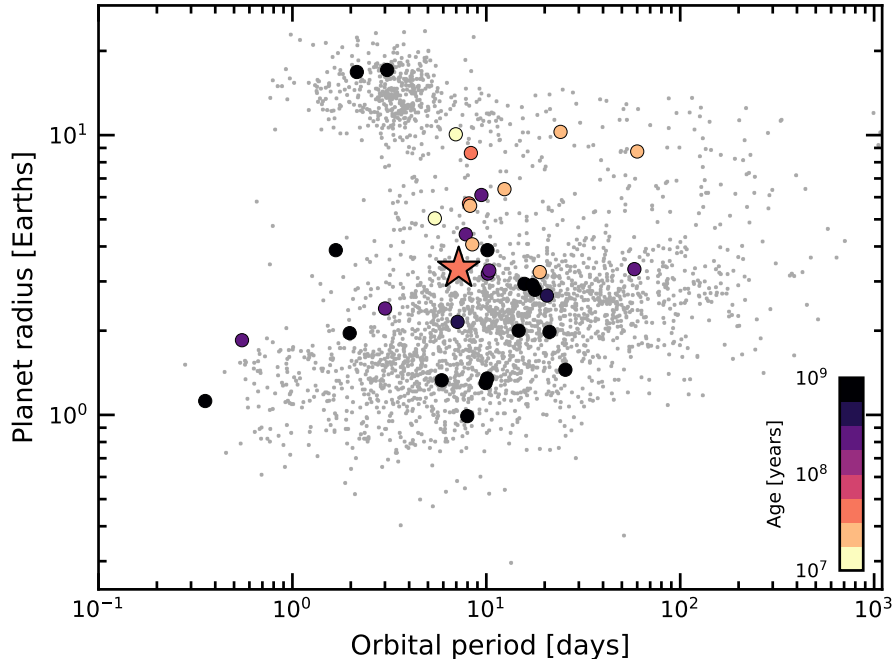


Figure 5. Radii, orbital periods, and ages of transiting exoplanets. Planets younger than a gigayear with $\tau/\sigma_\tau > 3$ are emphasized, where τ is the age and σ_τ is its uncertainty. Kepler 1627Ab is shown with a star. The large sizes of the youngest transiting planets could be explained by their primordial atmospheres not yet having evaporated; direct measurements of the atmospheric outflows or planetary masses would help to confirm this expectation. Selection effects may also be important. Parameters are from the NASA Exoplanet Archive (2021 Sept 15).

sits the primary star, which excludes a background eclipsing binary scenario, and therefore confirms that Kepler 1627Ab is a planet. It also suggests that the planet’s orbit is prograde. The latter point assumes that the dominant photometric variability is induced by dark spots, and not bright faculae. Given the observed transition of Sun-like stellar variability from spot to faculae-dominated regimes between young and old ages, we expect this assumption to be reasonably secure (Shapiro et al. 2016; Montet et al. 2017; Reinhold & Hekker 2020).

A third supporting line of evidence for the planetary interpretation also exists, though we consider it less definitive than the stellar density and TTV-local slope correlation. We observed a transit of Kepler 1627Ab on the night of 2021 Aug 7 simultaneously with Keck/HIRES and MuSCAT3. We scheduled the observations using the ephemeris of Holczer et al. (2016). Although we did not detect the Rossiter-McLaughlin (RM) anomaly, the multi-band MuSCAT3 light curves show the transit (Figure 4, lower panels). Fitting the MuSCAT3 photometry with a model that lets the transit depths vary across each bandpass, we find $griz$ depths consistent with the Kepler depth at 0.6, 0.3, 0.3, and 1.1σ respectively. The MuSCAT3 observations also suggest a transit duration 17.4 ± 3.6 minutes shorter than the Kepler transits; further photomet-

ric follow-up could help confirm whether the transit duration is indeed changing. For our RM analysis, the details are discussed in Appendix F. While the velocities are marginally more consistent with a prograde or polar orbit than a retrograde orbit, the spot-corrected exposure-to-exposure scatter ($\sigma_{RV} \approx 50 \text{ m s}^{-1}$) is larger than the expected velocity anomaly ($\Delta v_{RM} \approx 20 \text{ m s}^{-1}$). We are therefore not in a position to claim a spectroscopic detection of the RM effect, nor to quantify the stellar obliquity.

4. DISCUSSION & CONCLUSIONS

Kepler 1627Ab provides a new extremum in the ages of the Kepler planets, and opens multiple avenues for further study. Further observations of spectroscopic transits could yield a stellar obliquity measurement, which would confirm or refute the prograde orbital geometry suggested by the TTV-local slope correlation. Separately, transit spectroscopy aimed at detecting atmospheric outflows could yield insight into the evolutionary state of the atmosphere (e.g., Ehrenreich et al. 2015; Spake et al. 2018; Vissapragada et al. 2020). Observations aimed at quantifying the amount of high-energy irradiation incident on the planet would complement these efforts, by helping to clarify the expected outflow rate (e.g., Poppenhaeger et al. 2021). Finally, a challenging and informative quantity to measure would be the planet’s mass.

This might be possible through a high-cadence multi-color radial velocity campaign, or through long-term monitoring of the transit times and durations. Measured at sufficient precision, the mass, combined with the known age and size, would yield constraints on both the planet’s composition and its initial entropy (Owen 2020).

More immediately, the Kepler data may contain additional information. For instance, one possible explanation for the transit asymmetry shown in Figure 3 is that of a dusty asymmetric outflow. Other possible explanations such as favored longitudes for starspot crossings seem strained for reasons discussed in Appendix D. Dusty outflows are theoretically expected for young mini-Neptunes, and the amplitude of the observed asymmetry is also roughly consistent with predictions (Wang & Dai 2019). Beyond the planetary transits, Appendix G highlights a separate oddity in the Kepler data, in the arrival time distribution of stellar flares. We encourage its exploration by investigators more versed in the topic than ourselves.

In the context of the transiting planet population, Kepler 1627Ab is among the youngest known (Figure 5). Comparable systems with precise ages include K2-33, DS Tuc, HIP 67522, TOI 837, the two-planet AU Mic system, and the four-planet V1298 Tau system (Mann et al. 2016; David et al. 2016; Newton et al. 2019; David et al. 2019; Bouma et al. 2020; Plavchan et al. 2020; Martioli et al. 2021). Kepler 1627Ab is one of the smallest planets in this sample ($3.34 \pm 0.18 R_{\oplus}$), which could be linked to the selection effects imposed by the spot-induced photometric variability at very young ages (e.g., Zhou et al. 2021). Assuming that these young planets have masses between $\approx 5 M_{\oplus}$ and $10 M_{\oplus}$, their large sizes and presumed low densities would be in accord with the expectation that mini-Neptunes start their lives with large primordial atmospheres that are shed over the first gigayear (Owen & Wu 2013; Fulton et al. 2017; Ginzburg et al. 2018). The prograde orbit, if confirmed, would be consistent with a quiescent disk-driven migration history, and would differ from misalignments that have been observed for some older hot Neptunes (Sanchis-Ojeda & Winn 2011; Albrecht et al. 2012; Dalal et al. 2019; Rubenzahl et al. 2021).

Ultimately, the main advance of this work is a precise measurement of the age of Kepler 1627Ab. This measurement was enabled by identifying the connection of the star to the δ Lyr cluster using Gaia kinematics, and then by using the Gaia HR diagram and TESS stellar rotation periods to verify the cluster’s existence. Table 3 should enable similar cross-matches to already known planets, as well as forthcoming planets from TESS (Guerrero

et al. 2021). An alternative approach for age-dating more planets could be to identify kinematic associations around known exoplanet host stars using positions and tangential velocities from Gaia, and to then verify these associations with ancillary rotation periods and spectroscopy (e.g., Tofflemire et al. 2021).

ACKNOWLEDGMENTS

The authors are grateful to J. Winn, J. Spake, A. Howard, and T. David for illuminating discussions and suggestions, and to R. Kerr for kindly providing us with the Kerr et al. (2021) membership list prior to its publication. The authors are also grateful to K. Collins for helping resolve the scheduling conflict that would have otherwise prevented the MuSCAT3 observations. L.G.B. acknowledges support from a Charlotte Elizabeth Procter Fellowship from Princeton University, as well as from the TESS GI Program, programs G011103 and G022117, through NASA grants 80NSSC19K0386 and 80NSSC19K1728. Keck/NIRC2 imaging was acquired by program 2015A/N301N2L (PI: A. Kraus). In addition, this paper is based in part on observations made with the MuSCAT3 instrument, developed by the Astrobiology Center and under financial support by JSPS KAKENHI (JP18H05439) and JST PRESTO (JPMJPR1775), at Faulkes Telescope North on Maui, HI, operated by the Las Cumbres Observatory. This work is partly supported by JSPS KAKENHI Grant Numbers 22000005, JP15H02063, JP17H04574, JP18H05439, JP18H05442, JST PRESTO Grant Number JPMJPR1775, the Astrobiology Center of National Institutes of Natural Sciences (NINS) (Grant Number AB031010). This paper also includes data collected by the TESS mission, which are publicly available from the Mikulski Archive for Space Telescopes (MAST). Funding for the TESS mission is provided by NASA’s Science Mission directorate. We thank the TESS Architects (G. Ricker, R. Vanderspek, D. Latham, S. Seager, J. Jenkins) and the many TESS team members for their efforts to make the mission a continued success. Finally, this research has made use of the Keck Observatory Archive (KOA), which is operated by the W. M. Keck Observatory and the NASA Exoplanet Science Institute (NExScI), under contract with the National Aeronautics and Space Administration. We also thank the Keck Observatory staff for their support of HIRES and remote observing. We recognize the importance that the summit of Maunakea has within the indigenous Hawaiian community, and

are deeply grateful to have the opportunity to conduct observations from this mountain.

Software: altaipony (Ilin et al. 2021), astrobase (Bhatti et al. 2018), astropy (Astropy Collaboration et al. 2018), astroquery (Ginsburg et al. 2018), corner (Foreman-Mackey 2016), exoplanet (Foreman-Mackey et al. 2020), and its dependencies (Agol et al. 2020; Kipping 2013; Luger et al. 2019; Theano Development Team 2016), PyMC3 (Salvatier et al. 2016), scipy (Jones et al. 2001), TESS-point (Burke et al. 2020), wotan (Hippke et al. 2019).

Facilities: *Astrometry:* Gaia (Gaia Collaboration et al. 2018b, 2021a). *Imaging:* Second Generation Digitized Sky Survey. Keck:II (NIRC2; www2.keck.hawaii.edu/inst/nirc2). Gemini:North ('Alopeke; Scott et al. 2018, 2021). *Spectroscopy:* Keck:I (HIRES; Vogt et al. 1994). *Photometry:* Kepler (Borucki et al. 2010), MuSCAT3 (Narita et al. 2020), TESS (Ricker et al. 2015).

Table 1. Literature and Measured Properties for Kepler 1627

Primary Star			
TIC 120105470			
GAIADR2 [†] 2103737241426734336			
Parameter	Description	Value	Source
$\alpha_{J2015.5}$	Right Ascension (hh:mm:ss)	18:56:13.6	1
$\delta_{J2015.5}$	Declination (dd:mm:ss)	+41:34:36.22	1
V	Johnson V mag.	13.11 \pm 0.08	2
G	Gaia G mag.	13.02 \pm 0.02	1
G_{BP}	Gaia BP mag.	13.43 \pm 0.02	1
G_{RP}	Gaia RP mag.	12.44 \pm 0.02	1
T	TESS T mag.	12.53 \pm 0.02	2
J	2MASS J mag.	11.69 \pm 0.02	3
H	2MASS H mag.	11.30 \pm 0.02	3
K _s	2MASS K _s mag.	11.19 \pm 0.02	3
π	Gaia EDR3 parallax (mas)	3.009 \pm 0.032	1
d	Distance (pc)	329.5 \pm 3.5	1, 4
μ_α	Gaia EDR3 proper motion	1.716 \pm 0.034	1
	in RA (mas yr ⁻¹)		
μ_δ	Gaia EDR3 proper motion	-1.315 \pm 0.034	1
	in DEC (mas yr ⁻¹)		
RUWE	Gaia EDR3 renormalized	2.899	1
	unit weight error		
RV	Systemic radial velocity (km s ⁻¹)	-16.7 \pm 1.0	5
Spec. Type	Spectral Type	G8V	5
$v \sin i_*$	Rotational velocity* (km s ⁻¹)	18.9 \pm 1.0	5
Li EW	6708Å Equiv. Width (mÅ)	233 ⁺⁵ ₋₇	5
T_{eff}	Effective Temperature (K)	5505 \pm 60	6
$\log g_*$	Surface Gravity (cgs)	4.53 \pm 0.05	6
R_*	Stellar radius (R_\odot)	0.881 \pm 0.018	6
M_*	Stellar mass (R_\odot)	0.953 \pm 0.019	6
A_V	Interstellar reddening (mag)	0.2 \pm 0.1	6
[Fe/H]	Metallicity	0.1 \pm 0.1	6
P_{rot}	Rotation period (d)	2.642 \pm 0.042	7
Age	Adopted stellar age (Myr)	38 ⁺⁶ ₋₅	8
Δm_{832}	Mag difference ('Alopeke 832 nm)	3.14 \pm 0.04	9
θ_B	Position angle (deg)	91.9 \pm 0.7	9
ρ_B	Apparent separation of	0.164 \pm 0.010	9
	primary and secondary (as)		
ρ_B	Apparent separation of	53 \pm 4	1, 4, 9
	primary and secondary (AU)		
$\Delta m_{K'}$	Mag difference (NIRC2 K')	2.37 \pm 0.02	10
θ_B	Position angle (deg)	95.9 \pm 0.5	10
ρ_B	Apparent separation of	0.1739 \pm 0.0017	10
	primary and secondary (as)		

NOTE—[†] The GAIADR2 and GAIAEDR3 identifiers for Kepler 1627A are identical. The secondary is not resolved in the Gaia point source catalog. * Given only $v \sin i$ and $2\pi R_*/P_{\text{rot}}$, $\cos i = 0.11^{+0.11}_{-0.08}$. Provenances are: ¹Gaia Collaboration et al. (2021a), ²Stassun et al. (2019), ³Skrutskie et al. (2006), ⁴Lindgren et al. (2021), ⁵HIREs spectra and Yee et al. (2017), ⁶Cluster isochrone (MIST adopted; PARSEC compared for quoted uncertainty), ⁷Kepler light curve, ⁸Pre-main-sequence CAMD interpolation (Section 2.1), ⁹'Alopeke imaging 2021 June 24 (Scott et al. 2021), ¹⁰NIRC2 imaging 2015 July 22.

Table 2. Priors and Posteriors for Model Fitted to the Long Cadence Kepler 1627Ab Light Curve.

Param.	Unit	Prior	Median	Mean	Std. Dev.	3%	97%	ESS	$\hat{R} - 1$
<i>Sampled</i>									
P	d	$\mathcal{N}(7.20281; 0.01000)$	7.2028039	7.2028039	7.4e-06	7.2027901	7.202818	8673	0.0008753
$t_0^{(1)}$	d	$\mathcal{N}(120.79053; 0.02000)$	120.7904073	120.7904027	0.0009503	120.7886845	120.7922021	6349	0.0005352
$\log R_p/R_\star$	–	$\mathcal{U}(-4.605; 0.000)$	-3.36501	-3.36176	0.0406	-3.43579	-3.28478	2217	0.00138
b	–	$\mathcal{U}(0; 1 + R_p/R_\star)$	0.4638	0.4386	0.1994	0.0011	0.7415	1273	0.0015
u_1	–	Kipping (2013)	0.27	0.293	0.184	0.0	0.613	3534	0.001
u_2	–	Kipping (2013)	0.422	0.385	0.317	-0.213	0.901	3486	0.001
R_\star	R_\odot	$\mathcal{T}(0.881; 0.018)$	0.881	0.881	0.018	0.844	0.913	6920	-0.0
$\log g$	cgs	$\mathcal{N}(4.530; 0.050)$	4.531	4.532	0.051	4.438	4.628	7262	0.0
$\langle f \rangle$	–	$\mathcal{N}(0.500; 0.100)$	0.4999	0.4999	0.0001	0.4997	0.5	8553	0.0002
$e^{(2)}$	–	Van Eylen et al. (2019)	0.147	0.181	0.152	0.0	0.456	1954	0.001
ω	rad	$\mathcal{U}(0.000; 6.283)$	0.097	0.058	1.84	-2.867	3.141	3805	0.001
$\log \sigma_f$	–	$\mathcal{N}(\log \langle \sigma_f \rangle; 2.000)$	-8.034	-8.034	0.008	-8.048	-8.02	7639	0.0
σ_{rot}	d^{-1}	InvGamma(1.000; 5.000)	0.07	0.07	0.001	0.068	0.072	8198	0.001
$\log P_{\text{rot}}$	$\log(d)$	$\mathcal{N}(0.958; 0.020)$	0.978	0.978	0.001	0.975	0.98	7991	0.0
$\log Q_0$	–	$\mathcal{N}(0.000; 2.000)$	-0.325	-0.325	0.043	-0.407	-0.246	8304	0.002
$\log dQ$	–	$\mathcal{N}(0.000; 2.000)$	7.699	7.697	0.103	7.505	7.888	8140	0.001
f	–	$\mathcal{U}(0.010; 1.000)$	0.01	0.01	0.0	0.01	0.01	5097	0.002
R_p/R_\star	–	–	0.035	0.035	0.001	0.032	0.037	2217	0.001
ρ_\star	g cm^{-3}	–	1.984	2.001	0.236	1.573	2.45	7248	0.0
R_p	R_{Jup}	–	0.297	0.298	0.016	0.269	0.33	3047	0.001
R_p	R_{Earth}	–	3.329	3.34	0.179	3.015	3.699	3047	0.001
a/R_\star	–	–	17.589	17.611	0.691	16.28	18.87	7247	0.0
$\cos i$	–	–	0.027	0.025	0.01	0.003	0.039	1435	0.002
T_{14}	hr	–	2.825	2.826	0.057	2.717	2.927	4099	0.001
T_{13}	hr	–	2.575	2.562	0.086	2.415	2.71	2190	-0.0

NOTE— ESS refers to the number of effective samples. \hat{R} is the Gelman-Rubin convergence diagnostic. Logarithms through this table are in base-e. \mathcal{U} denotes a uniform distribution, \mathcal{N} a normal distribution, and \mathcal{T} a truncated normal bounded between zero and an upper limit much larger than the mean.

(1) The ephemeris is in units of BJDTDB - 2454833. (2) The eccentricity vectors are sampled in the $(e \cos \omega, e \sin \omega)$ basis.

Table 3. Young, Age-dated, and Age-dateable Stars Within the Nearest Few Kiloparsecs.

Parameter	Example Value	Description
source_id	1709456705329541504	Gaia DR2 source identifier.
ra	247.826	Gaia DR2 right ascension [deg].
dec	79.789	Gaia DR2 declination [deg].
parallax	35.345	Gaia DR2 parallax [mas].
parallax_error	0.028	Gaia DR2 parallax uncertainty [mas].
pmra	94.884	Gaia DR2 proper motion $\mu_\alpha \cos \delta$ [mas yr $^{-1}$].
pmdec	-86.971	Gaia DR2 proper motion μ_δ [mas yr $^{-1}$].
phot_g_mean_mag	6.85	Gaia DR2 G magnitude.
phot_bp_mean_mag	6.409	Gaia DR2 G_{BP} magnitude.
phot_rp_mean_mag	7.189	Gaia DR2 G_{RP} magnitude.
cluster	NASAExoArchive_ps_20210506,Uma,IR_excess	Comma-separated cluster or group name.
age	9.48,nan,nan	Comma-separated logarithm (base-10) of reported ^a age in years.
mean_age	9.48	Mean (ignoring NaNs) of age column.
reference_id	NASAExoArchive_ps_20210506,Ujjwal2020,CottenSong2016	Comma-separated provenance of group membership.
reference_bibcode	2013PASP..125..989A,2020AJ....159..166U,2016ApJS..225..15C	ADS bibcode corresponding to reference_id.

NOTE— Table 3 is published in its entirety in a machine-readable format. This table is a concatenation of the studies listed in Table 4. One entry is shown for guidance regarding form and content. In this particular example, the star has a cold Jupiter on a 16 year orbit, HD 150706b (Boisse et al. 2012). An infrared excess has been reported (Cotten & Song 2016), and the star was identified by Ujjwal et al. (2020) as a candidate UMa moving group member (≈ 400 Myr; Mann et al. 2020). The star's RV activity and TESS rotation period corroborate its youth.

Table 4. Provenances of Young and Age-dateable Stars.

Reference	N_{Gaia}	N_{Age}	$N_{G_{\text{RP}} < 16}$
Kounkel et al. (2020)	987376	987376	775363
Cantat-Gaudin & Anders (2020)	433669	412671	269566
Cantat-Gaudin et al. (2018)	399654	381837	246067
Kounkel & Covey (2019)	288370	288370	229506
Cantat-Gaudin et al. (2020)	233369	227370	183974
Zari et al. (2018) UMS	86102	0	86102
Wenger et al. (2000) Y*?	61432	0	45076
Zari et al. (2018) PMS	43719	0	38435
Gaia Collaboration et al. (2018a) $d > 250 \text{ pc}$	35506	31182	18830
Castro-Ginard et al. (2020)	33635	24834	31662
Kerr et al. (2021)	30518	25324	27307
Wenger et al. (2000) Y*○	28406	0	16205
Villa Vélez et al. (2018)	14459	14459	13866
Cantat-Gaudin et al. (2019)	11843	11843	9246
Damiani et al. (2019) PMS	10839	10839	9901
Oh et al. (2017)	10379	0	10370
Meingast et al. (2021)	7925	7925	5878
Wenger et al. (2000) pMS*	5901	0	3006
Gaia Collaboration et al. (2018a) $d < 250 \text{ pc}$	5378	817	3968
Kounkel et al. (2018)	5207	3740	5207
Ratzenböck et al. (2020)	4269	4269	2662
Wenger et al. (2000) TT*	4022	0	3344
Damiani et al. (2019) UMS	3598	3598	3598
Rizzuto et al. (2017)	3294	3294	2757
Akeson et al. (2013)	3107	868	3098
Tian (2020)	1989	1989	1394
Goldman et al. (2018)	1844	1844	1783
Cotten & Song (2016)	1695	0	1693
Gagné et al. (2018b)	1429	0	1389
Röser & Schilbach (2020) Psc-Eri	1387	1387	1107
Röser & Schilbach (2020) Pleiades	1245	1245	1019
Wenger et al. (2000) TT?	1198	0	853
Gagné & Faherty (2018)	914	0	913
Pavlidou et al. (2021)	913	913	504
Gagné et al. (2018a)	692	0	692
Ujjwal et al. (2020)	563	0	563
Gagné et al. (2020)	566	566	351
Esplin & Luhman (2019)	377	443	296
Roccatagliata et al. (2020)	283	283	232
Meingast & Alves (2019)	238	238	238
Fürnkranz et al. (2019) Coma-Ber	214	214	213
Fürnkranz et al. (2019) Neighbor Group	177	177	167
Kraus et al. (2014)	145	145	145

NOTE— Table 4 describes the provenances for the young and age-dateable stars in Table 3. N_{Gaia} : number of Gaia stars we parsed from the literature source. N_{Age} : number of stars in the literature source with ages reported. $N_{G_{\text{RP}} < 16}$: number of Gaia stars we parsed from the literature source with either $G_{\text{RP}} < 16$, or a parallax S/N exceeding 5 and a distance closer than 100 pc. The latter criterion included a few hundred white dwarfs that would have otherwise been neglected. Some studies are listed multiple times if they contain multiple tables. Wenger et al. (2000) refers to the SIMBAD database.

REFERENCES

- Agol, E., Luger, R., & Foreman-Mackey, D. 2020, *AJ*, **159**, 123
- Akeson, R. L., Chen, X., Ciardi, D., et al. 2013, *PASP*, **125**, 989
- Albrecht, S., Winn, J. N., Johnson, J. A., et al. 2012, *ApJ*, **757**, 18
- Astropy Collaboration, Price-Whelan, A. M., Sipőcz, B. M., et al. 2018, *AJ*, **156**, 123
- Baraffe, I., Homeier, D., Allard, F., & Chabrier, G. 2015, *A&A*, **577**, A42
- Beaumont, C., Robitaille, T., Borkin, M., & Goodman, A. 2014, glueviz v0.4: multidimensional data exploration
- Berger, T. A., Howard, A. W., & Boesgaard, A. M. 2018, *ApJ*, **855**, 115
- Bhatti, W., Bouma, L. G., & Wallace, J. 2018, astrobase, <https://doi.org/10.5281/zenodo.1469822>
- Boisse, I., Pepe, F., Perrier, C., et al. 2012, *A&A*, **545**, A55
- Borucki, W. J., Koch, D., Basri, G., et al. 2010, *Science*, **327**, 977
- Bossini, D., Vallenari, A., Bragaglia, A., et al. 2019, *A&A*, **623**, A108
- Bouma, L. G., Curtis, J. L., Hartman, J. D., Winn, J. N., & Bakos, G. A. 2021, arXiv:2107.08050 [astro-ph]
- Bouma, L. G., Hartman, J. D., Bhatti, W., Winn, J. N., & Bakos, G. Á. 2019, *ApJS*, **245**, 13
- Bouma, L. G., Hartman, J. D., Brahm, R., et al. 2020, *AJ*, **160**, 239
- Bressan, A., Marigo, P., Girardi, L., et al. 2012, *MNRAS*, **427**, 127
- Burke, C. J., Levine, A., Fausnaugh, M., et al. 2020, TESS-Point: High precision TESS pointing tool, Astrophysics Source Code Library, [ascl:2003.001](https://ascl.net/2003.001)
- Cantat-Gaudin, T., & Anders, F. 2020, *A&A*, **633**, A99
- Cantat-Gaudin, T., Jordi, C., Vallenari, A., et al. 2018, *A&A*, **618**, A93
- Cantat-Gaudin, T., Jordi, C., Vallenari, A., et al. 2018, *A&A*, **618**, A93
- Cantat-Gaudin, T., Jordi, C., Wright, N. J., et al. 2019, *A&A*, **626**, A17
- Cantat-Gaudin, T., Anders, F., Castro-Ginard, A., et al. 2020, *A&A*, **640**, A1
- Capitanio, L., Lallement, R., Vergely, J. L., Elyajouri, M., & Monreal-Ibero, A. 2017, *A&A*, **606**, A65
- Castro-Ginard, A., Jordi, C., Luri, X., et al. 2020, *A&A*, **635**, A45
- Chabrier, G., Baraffe, I., Allard, F., & Hauschildt, P. 2000, *ApJ*, **542**, 464
- Choi, J., Dotter, A., Conroy, C., et al. 2016, *ApJ*, **823**, 102
- Claret, A., & Bloemen, S. 2011, *A&A*, **529**, A75
- Cotten, T. H., & Song, I. 2016, *ApJS*, **225**, 15
- Dahm, S. E. 2015, *ApJ*, **813**, 108
- Dai, F., Winn, J. N., Berta-Thompson, Z., Sanchis-Ojeda, R., & Albrecht, S. 2018, *AJ*, **155**, 177
- Dalal, S., Hébrard, G., Lecavelier des Étangs, A., et al. 2019, *A&A*, **631**, A28
- Damiani, F., Prisinzano, L., Pillitteri, I., Micela, G., & Sciortino, S. 2019, *A&A*, **623**, A112
- Damiani, F., Prisinzano, L., Pillitteri, I., Micela, G., & Sciortino, S. 2019, *A&A*, **623**, A112
- Davenport, J. R. A. 2016, *ApJ*, **829**, 23
- Davenport, J. R. A., Hawley, S. L., Hebb, L., et al. 2014, *ApJ*, **797**, 122
- David, T., Hillenbrand, L., & Petigura, E. 2016, *Nature*, **534**, 658
- David, T. J., & Hillenbrand, L. A. 2015, *ApJ*, **804**, 146
- David, T. J., Petigura, E. A., Luger, R., et al. 2019, *ApJL*, **885**, L12
- David, T. J., Contardo, G., Sandoval, A., et al. 2021, *AJ*, **161**, 265
- Dias, W. S., Monteiro, H., Caetano, T. C., et al. 2014, *A&A*, **564**, A79
- Dobbie, P. D., Lodieu, N., & Sharp, R. G. 2010, *MNRAS*, **409**, 1002
- Douglas, S. T., Agüeros, M. A., Covey, K. R., & Kraus, A. 2017, *ApJ*, **842**, 83
- Douglas, S. T., Pérez Chávez, J., Cargile, P. A., et al. 2021, Constraining Stellar Rotation at the ZAMS
- Eggen, O. J. 1968, *ApJ*, **152**, 77
- Ehrenreich, D., Bourrier, V., Wheatley, P. J., et al. 2015, *Nature*, **522**, 459
- Esplin, T. L., & Luhman, K. L. 2019, *AJ*, **158**, 54
- Foreman-Mackey, D. 2016, *Journal of Open Source Software*, **1**, 24
- Foreman-Mackey, D., Czekala, I., Luger, R., et al. 2020, exoplanet-dev/exoplanet v0.2.6
- Fulton, B. J., Petigura, E. A., Howard, A. W., et al. 2017, *AJ*, **154**, 109
- Fürnkranz, V., Meingast, S., & Alves, J. 2019, *A&A*, **624**, L11
- Gagné, J., David, T. J., Mamajek, E. E., et al. 2020, *ApJ*, **903**, 96
- Gagné, J., & Faherty, J. K. 2018, *ApJ*, **862**, 138

- Gagné, J., Roy-Loubier, O., Faherty, J. K., Doyon, R., & Malo, L. 2018a, *ApJ*, **860**, 43
- Gagné, J., Mamajek, E. E., Malo, L., et al. 2018b, *ApJ*, **856**, 23
- Gagné, J., David, T. J., Mamajek, E. E., et al. 2020, *ApJ*, **903**, 96
- Gaia Collaboration, Babusiaux, C., van Leeuwen, F., et al. 2018a, *A&A*, **616**, A10
- Gaia Collaboration, Brown, A. G. A., Vallenari, A., et al. 2018b, *A&A*, **616**, A1
- . 2021a, *A&A*, **649**, A1
- Gaia Collaboration, Smart, R. L., Sarro, L. M., et al. 2021b, *A&A*, **649**, A6
- Gelman, A., & Rubin, D. B. 1992, *Statistical Science*, **7**, 457, publisher: Institute of Mathematical Statistics
- Gillen, E., Briegal, J. T., Hodgkin, S. T., et al. 2020, *MNRAS*, **492**, 1008
- Ginsburg, A., Sipocz, B., Madhura Parikh, et al. 2018, *Astropy/Astroquery: V0.3.7 Release*
- Ginzburg, S., Schlichting, H. E., & Sari, R. 2018, *MNRAS*, **476**, 759
- Goldman, B., Röser, S., Schilbach, E., Moór, A. C., & Henning, T. 2018, *ApJ*, **868**, 32
- Guerrero, N. M., Seager, S., Huang, C. X., et al. 2021, *arXiv:2103.12538 [astro-ph]*
- Günther, M. N., Zhan, Z., Seager, S., et al. 2020, *AJ*, **159**, 60
- Hattori, S., Foreman-Mackey, D., Hogg, D. W., et al. 2021, arXiv e-prints, arXiv:2106.15063
- Hippke, M., David, T. J., Mulders, G. D., & Heller, R. 2019, *AJ*, **158**, 143
- Hirano, T., Suto, Y., Taruya, A., et al. 2010, *ApJ*, **709**, 458
- Hirano, T., Suto, Y., Winn, J. N., et al. 2011, *ApJ*, **742**, 69, aDS Bibcode: 2011ApJ...742...69H
- Hoffman, M. D., & Gelman, A. 2014, *Journal of Machine Learning Research*, **15**, 1593
- Holczer, T., Shporer, A., Mazeh, T., et al. 2015, *ApJ*, **807**, 170
- Holczer, T., Mazeh, T., Nachmani, G., et al. 2016, *ApJS*, **225**, 9
- Howard, A. W., Johnson, J. A., Marcy, G. W., et al. 2010, *ApJ*, **721**, 1467
- Howell, S. B., Everett, M. E., Sherry, W., Horch, E., & Ciardi, D. R. 2011, *AJ*, **142**, 19
- Ilin, E., Schmidt, S. J., Poppenh̄ger, K., et al. 2021, *A&A*, **645**, A42
- Jones, E., Oliphant, T., Peterson, P., et al. 2001, Open source scientific tools for Python
- Jontof-Hutter, D., Wolfgang, A., Ford, E. B., et al. 2021, *AJ*, **161**, 246
- Kerr, R., Rizzuto, A. C., Kraus, A. L., & Offner, S. S. R. 2021, *arXiv:2105.09338 [astro-ph]*
- Kharchenko, N. V., Piskunov, A. E., Schilbach, E., Röser, S., & Scholz, R.-D. 2013, *A&A*, **558**, A53
- Kipping, D. M. 2010, *MNRAS*, **408**, 1758
- Kipping, D. M. 2013, *MNRAS*, **435**, 2152
- Kite, E. S., Fegley, Jr., B., Schaefer, L., & Ford, E. B. 2020, *ApJ*, **891**, 111
- Klein, B., & Donati, J.-F. 2020, *MNRAS*, **493**, L92, publisher: Oxford Academic
- Kounkel, M., & Covey, K. 2019, *AJ*, **158**, 122
- Kounkel, M., & Covey, K. 2019, *AJ*, **158**, 122
- Kounkel, M., Covey, K., & Stassun, K. G. 2020, *AJ*, **160**, 279
- Kounkel, M., Covey, K., Suárez, G., et al. 2018, *AJ*, **156**, 84
- Kounkel, M., Covey, K., Suárez, G., et al. 2018, *AJ*, **156**, 84
- Kraus, A. L., Ireland, M. J., Huber, D., Mann, A. W., & Dupuy, T. J. 2016, *AJ*, **152**, 8
- Kraus, A. L., Shkolnik, E. L., Allers, K. N., & Liu, M. C. 2014, *AJ*, **147**, 146
- Lallement, R., Capitanio, L., Ruiz-Dern, L., et al. 2018, *A&A*, **616**, A132
- Lindgren, L., Bastian, U., Biermann, M., et al. 2021, *A&A*, **649**, A4
- Lomb, N. R. 1976, *Astrophysics and Space Science*, **39**, 447
- Luger, R., Agol, E., Foreman-Mackey, D., et al. 2019, *AJ*, **157**, 64
- Mann, A. W., Newton, E. R., Rizzuto, A. C., et al. 2016, *AJ*, **152**, 61
- Mann, A. W., Johnson, M. C., Vanderburg, A., et al. 2020, *AJ*, **160**, 179
- Martioli, E., Hébrard, G., Correia, A. C. M., Laskar, J., & Lecavelier des Etangs, A. 2021, *A&A*, **649**, A177
- Masuda, K. 2015, *ApJ*, **805**, 28
- Mazeh, T., Holczer, T., & Shporer, A. 2015, *ApJ*, **800**, 142
- McCann, J., Murray-Clay, R. A., Kratter, K., & Krumholz, M. R. 2019, *ApJ*, **873**, 89
- McKinney, W. 2010, in Proceedings of the 9th Python in Science Conference, ed. S. van der Walt & J. Millman, 51
- McQuillan, A., Mazeh, T., & Aigrain, S. 2014, *ApJS*, **211**, 24
- Meibom, S., Mathieu, R. D., & Stassun, K. G. 2007, *ApJL*, **665**, L155
- Meibom, S., Barnes, S. A., Latham, D. W., et al. 2011, *ApJL*, **733**, L9

- Meibom, S., Torres, G., Fressin, F., et al. 2013, *Nature*, **499**, 55
- Meingast, S., & Alves, J. 2019, *A&A*, **621**, L3
- Meingast, S., Alves, J., & Rottensteiner, A. 2021, *A&A*, **645**, A84
- Montet, B. T., Tovar, G., & Foreman-Mackey, D. 2017, *ApJ*, **851**, 116
- Montet, B. T., Feinstein, A. D., Luger, R., et al. 2020, *AJ*, **159**, 112
- Morris, B. M. 2020, *ApJ*, **893**, 67
- Morton, T. D., Bryson, S. T., Coughlin, J. L., et al. 2016, *ApJ*, **822**, 86
- Narita, N., Fukui, A., Yamamuro, T., et al. 2020, in *SPIE Conference Series, Vol. 11447, SPIE Conference Series*, 114475K
- Newton, E. R., Mann, A. W., Tofflemire, B. M., et al. 2019, *ApJ*, **880**, L17
- Oh, S., Price-Whelan, A. M., Hogg, D. W., Morton, T. D., & Spergel, D. N. 2017, *AJ*, **153**, 257
- Owen, J. E. 2020, arXiv:2009.03919 [astro-ph]
- Owen, J. E., & Wu, Y. 2013, *ApJ*, **775**, 105
- . 2016, *ApJ*, **817**, 107
- Palle, E., Oshagh, M., Casasayas-Barris, N., et al. 2020, *A&A*, **643**, 25
- Pavlidou, T., Scholz, A., & Teixeira, P. S. 2021, *MNRAS*, **503**, 3232
- Pecaut, M. J., & Mamajek, E. E. 2013, *ApJS*, **208**, 9
- Pecaut, M. J., & Mamajek, E. E. 2016, *MNRAS*, **461**, 794
- Plavchan, P., Barclay, T., Gagné, J., et al. 2020, *Nature*, **582**, 497
- Poppenhaeger, K., Ketzer, L., & Mallonn, M. 2021, *MNRAS*, **500**, 4560
- Randich, S., Tognelli, E., Jackson, R., et al. 2018, *A&A*, **612**, A99
- Ratzenböck, S., Meingast, S., Alves, J., Möller, T., & Bomze, I. 2020, *A&A*, **639**, A64
- Rebull, L. M., Stauffer, J. R., Bouvier, J., et al. 2016, *AJ*, **152**, 113
- Reinhold, T., & Hekker, S. 2020, *A&A*, **635**, A43
- Ricker, G. R., Winn, J. N., Vanderspek, R., et al. 2015, *JATIS*, **1**, 014003
- Rizzuto, A. C., Mann, A. W., Vanderburg, A., Kraus, A. L., & Covey, K. R. 2017, *ApJ*, **154**, 224
- Rizzuto, A. C., Newton, E. R., Mann, A. W., et al. 2020, arXiv:2005.00013 [astro-ph]
- Roccatagliata, V., Franciosini, E., Sacco, G. G., Randich, S., & Sicilia-Aguilar, A. 2020, *A&A*, **638**, A85
- Roettenbacher, R. M., Monnier, J. D., Korhonen, H., et al. 2017, *ApJ*, **849**, 120
- Röser, S., & Schilbach, E. 2020, *A&A*, **638**, A9
- Rowe, J. F., Bryson, S. T., Marcy, G. W., et al. 2014, *ApJ*, **784**, 45
- Rubenzahl, R. A., Dai, F., Howard, A. W., et al. 2021, *AJ*, **161**, 119
- Salvatier, J., Wiecki, T. V., & Fonnesbeck, C. 2016, PyMC3: Python probabilistic programming framework
- Sanchis-Ojeda, R., & Winn, J. N. 2011, *ApJ*, **743**, 61
- Scargle, J. D. 1982, *ApJ*, **263**, 835
- Scott, N. J., Howell, S. B., Horch, E. P., & Everett, M. E. 2018, *PASP*, **130**, 054502
- Scott, N. J., Howell, S. B., Gnilka, C. L., et al. 2021, *Frontiers in Astronomy and Space Sciences*, **8**, 138
- Shapiro, A. I., Solanki, S. K., Krivova, N. A., Yeo, K. L., & Schmutz, W. K. 2016, *A&A*, **589**, A46
- Skrutskie, M. F., Cutri, R. M., Stiening, R., et al. 2006, *AJ*, **131**, 1163
- Soderblom, D. R., Hillenbrand, L. A., Jeffries, R. D., Mamajek, E. E., & Naylor, T. 2014, *Protostars and Planets VI*, 219
- Spake, J. J., Sing, D. K., Evans, T. M., et al. 2018, *Nature*, **557**, 68
- Stassun, K. G., Oelkers, R. J., Paegert, M., et al. 2019, *AJ*, **158**, 138
- Stauffer, J., Rebull, L., Bouvier, J., et al. 2016, *AJ*, **152**, 115
- Stauffer, J. R., Hartmann, L. W., Prosser, C. F., et al. 1997, *ApJ*, **479**, 776
- Stefansson, G., Mahadevan, S., Maney, M., et al. 2020, *AJ*, **160**, 192
- Stephenson, C. B. 1959, *PASP*, **71**, 145
- Strassmeier, K. G. 2009, *Astronomy and Astrophysics Review*, **17**, 251
- Tenenbaum, P., Christiansen, J. L., Jenkins, J. M., et al. 2012, *ApJS*, **199**, 24
- Theano Development Team. 2016, arXiv e-prints, abs/1605.02688
- Thompson, S. E., Coughlin, J. L., Hoffman, K., et al. 2018, *ApJS*, **235**, 38
- Tian, H.-J. 2020, *ApJ*, **904**, 196
- Tofflemire, B. M., Rizzuto, A. C., Newton, E. R., et al. 2021, *AJ*, **161**, 171
- Ujjwal, K., Kartha, S. S., Mathew, B., Manoj, P., & Narang, M. 2020, *AJ*, **159**, 166
- Van Eylen, V., Albrecht, S., Huang, X., et al. 2019, *AJ*, **157**, 61
- Villa Vélez, J. A., Brown, A. G. A., & Kenworthy, M. A. 2018, *RNAAS*, **2**, 58
- Vissapragada, S., Knutson, H. A., Jovanovic, N., et al. 2020, *AJ*, **159**, 278

- Vogt, S. S., Allen, S. L., Bigelow, B. C., et al. 1994,
SPIE Conference Series, ed. D. L. Crawford & E. R.
Craine, Vol. 2198
- Wang, L., & Dai, F. 2019, [ApJL](#), 873, L1
- Wenger, M., Ochsenbein, F., Egret, D., et al. 2000,
[A&AS](#), 143, 9
- Wirth, C. P., Zhou, G., Quinn, S. N., et al. 2021, [ApJL](#),
917, L34
- Yee, S. W., Petigura, E. A., & von Braun, K. 2017, [ApJ](#),
836, 77
- Yelda, S., Lu, J. R., Ghez, A. M., et al. 2010, [ApJ](#), 725,
331
- Zari, E., Hashemi, H., Brown, A. G. A., Jardine, K., &
de Zeeuw, P. T. 2018, [A&A](#), 620, A172
- Zari, E., Hashemi, H., Brown, A. G. A., Jardine, K., &
de Zeeuw, P. T. 2018, [A&A](#), 620, A172
- Zhou, G., Winn, J. N., Newton, E. R., et al. 2020, [ApJ](#),
892, L21
- Zhou, G., Quinn, S. N., Irwin, J., et al. 2021, [AJ](#), 161, 2

APPENDIX

A. YOUNG, AGE-DATED, AND AGE-DATEABLE STAR COMPILATION

The v0.6 CDIPS target catalog (Table 3) includes stars that are young, age-dated, and age-dateable. By “age-dateable”, we mean that the age should be measurable at greater precision than a typical FGK field star using isochronal, gyrochronal, or spectroscopic techniques. As in Bouma et al. (2019), we collected stars that met these criteria from across the literature. Table 4 gives a list of the studies included, and brief summary statistics. The age measurement methodologies adopted by each study differ: in many, spatial and kinematic clustering has been performed on the Gaia data, and ensemble isochrone fitting of the resulting clusters has been performed (typically focusing on the turn-off). In other studies however, the claim of youth is based on the location of a single star in the color-absolute magnitude diagram, or on spectroscopic information.

One major change in Table 3 relative to the analogous table from Bouma et al. (2019) is that the extent of Gaia-based analyses has now matured to the point that we can neglect pre-Gaia cluster memberships, except for a few cases with spectroscopically confirmed samples of age-dated stars. The membership lists for instance of Kharchenko et al. (2013) and Dias et al. (2014) (MWSC and DAML) are no longer required. This is helpful for various post-processing projects, since the field-star contamination rates were typically much higher than analogous Gaia-based cluster membership catalogs.

The most crucial parameters of a given star for our purposes are the Gaia DR2 `source_id`, the cluster or group name (`cluster`), and the `age`. Given the hierarchical nature of many stellar associations, we do not attempt to resolve the cluster names to a single unique string. The Orion complex for instance can be divided into almost one hundred kinematic subgroups (Kounkel et al. 2018). Similar complexity applies to the problem of determining homogeneous ages, which we do not attempt to resolve. Instead, we simply merged the cluster names and ages reported by various authors into a comma-separated string.

This means that the `age` column can be null, for cases in which the original authors did not report an age, or for which a reference literature age was not readily available. Nonetheless, since we do generally prefer stars with known ages, we made a few additional efforts to populate this column. When available, the age provenance is from the original analysis of the cluster. In a few cases however we adopted other ages when string-based cross-matching on the cluster name was straightforward. In particular, we used the ages determined by Cantat-Gaudin et al. (2020) to assign ages to the clusters from Gaia Collaboration et al. (2018a), Cantat-Gaudin et al. (2018), Castro-Ginard et al. (2020), and Cantat-Gaudin & Anders (2020).

The catalogs we included for which ages were not immediately available were those of Cotten & Song (2016), Oh et al. (2017), Zari et al. (2018), Gagné et al. (2018a), Gagné et al. (2018b), Gagné & Faherty (2018), and Ujjwal et al. (2020). While in principle the moving group members discussed by Gagné et al. (2018a,b); Gagné & Faherty (2018) and Ujjwal et al. (2020) have easily associated ages, our SIMBAD cross-match did not retain the moving group identifiers given by those studies, which should therefore be recovered using tools such as BANYAN Σ ⁶. We also included the SIMBAD object identifiers TT*, Y*O,Y*?, TT?, and pMS*. Finally, we included every star in the NASA Exoplanet Archive planetary system (ps) table that had a Gaia identifier available (Akeson et al. 2013). If the age had finite uncertainties, we also included it, since stellar ages determined through the combination of isochrone-fitting and transit-derived stellar densities typically have higher precision than from isochrones alone.

For any of the catalogs for which Gaia DR2 identifiers were not immediately available, we either followed the spatial (plus proper-motion) cross-matching procedures described in Bouma et al. (2019), or else we pulled the Gaia DR2 source identifiers associated with the catalog from SIMBAD. We consequently opted to drop the `ext_catalog_name` and `dist` columns maintained in Bouma et al. (2019), as these were only populated for a small number of stars. The technical manipulations for the merging, cleaning, and joining were performed using pandas (McKinney 2010). The eventual cross-match (using the Gaia DR2 `source_id`) against the Gaia DR2 archive was performed asynchronously on the Gaia archive website⁷.

B. KINEMATIC SELECTION OF δ LYR CLUSTER MEMBERS

Figure 6 shows stars reported by Kounkel & Covey (2019) to be in the group “Theia 73”, which was cross-matched by Kounkel & Covey as being “Stephenson 1”. Kounkel & Covey (2019) reported 3,071 stars to be present in this cluster. For our Figure, galactic positions were calculated and plotted only for stars

⁶ <http://www.exoplanetes.umontreal.ca/banyan/banyansigma.php>

⁷ <https://gea.esac.esa.int/archive/>

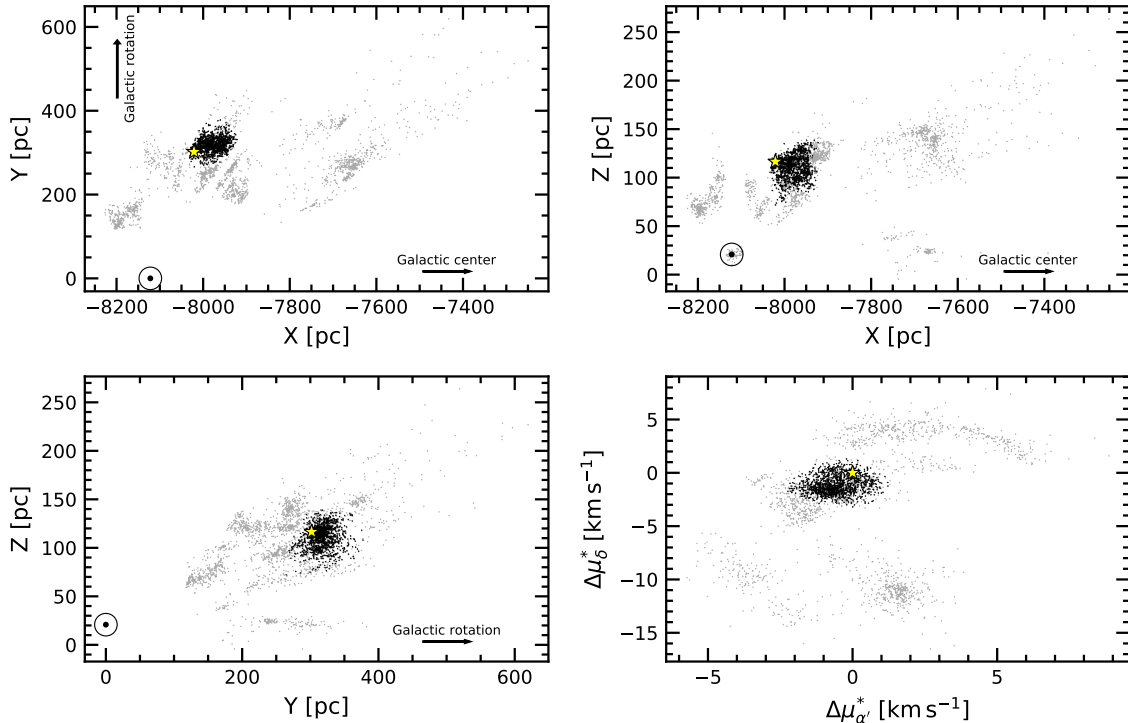


Figure 6. Galactic position and tangential velocities of the δ Lyr cluster. Points are candidate cluster members with $\bar{\omega}/\sigma_{\bar{\omega}} > 20$, reported to be in the group by Kounkel & Covey (2019). We focus on stars in a small region (black points) in the kinematic vicinity of Kepler 1627 (yellow star). The other candidate cluster members (gray points) may or may not share the ages of the selected kinematic group. The location of the Sun is (\odot) is shown.

with parallax signal-to-noise exceeding 20. The location of the Sun is shown on the plots. The smattering of reported cluster members (gray and black points) has a significantly different structure than the cluster initially identified by Stephenson (1959) and corroborated by Eggen (1968). While the non-uniform “clumps” might be part of a real structure, they could also be an artifact of the data processing steps performed by Kounkel & Covey (2019). We therefore opted to only consider stars in the immediate kinematic and spatial vicinity of Kepler 1627. The tangential velocities relative to Kepler 1627 are shown in the bottom right panel. These are computed by assuming that every star has the same three-dimensional spatial velocity as Kepler 1627, where we assume a systemic radial velocity of $-16.7 \pm 0.2 \text{ km s}^{-1}$ based on the HIRES spectra. The relevant projection effects are then taken into account, as discussed by *e.g.*, Meingast et al. (2021) and Bouma et al. (2021). We performed the actual selection by then manually drawing lassos with the interactive glue visualization tool (Beaumont et al. 2014) in the four projections shown in Figure 6. While other cluster members likely exist outside of our selection region (and our selection also includes some field star interlopers), our aim is to verify the existence of the cluster in the vicinity of Kepler 1627, and to measure its age. The procedure we have adopted enables both tasks.

C. BINARITY AND STELLAR ROTATION FOR δ LYR CLUSTER MEMBERS

Figure 7 shows the rotation-color diagram for δ Lyr cluster members, with the points colored according to indicators of binarity. The binaries tend to be redder and have shorter rotation periods. We know of two possible explanations based on selection effects, and two based on physics.

Possible selection effects include *i*) binaries have a component that contributes additional red light to the system, which could skew the color measurement of the primary; and *ii*) the unresolved binary companions could contaminate the rotation period measurement (*e.g.*, Stauffer et al. 2016, Section 5.1).

The two possible physical effects that could be relevant are tidal locking and pre-main-sequence disk locking. Tidal locking has been argued to be an unlikely explanation for the frequency of rapid rotators due to the population statistics; a more likely scenario would be that the presence of the binary leads to faster disk dispersal, enabling the primary to contract to more rapid rotation periods than possible for single stars (Meibom et al. 2007; Bouma et al. 2020).

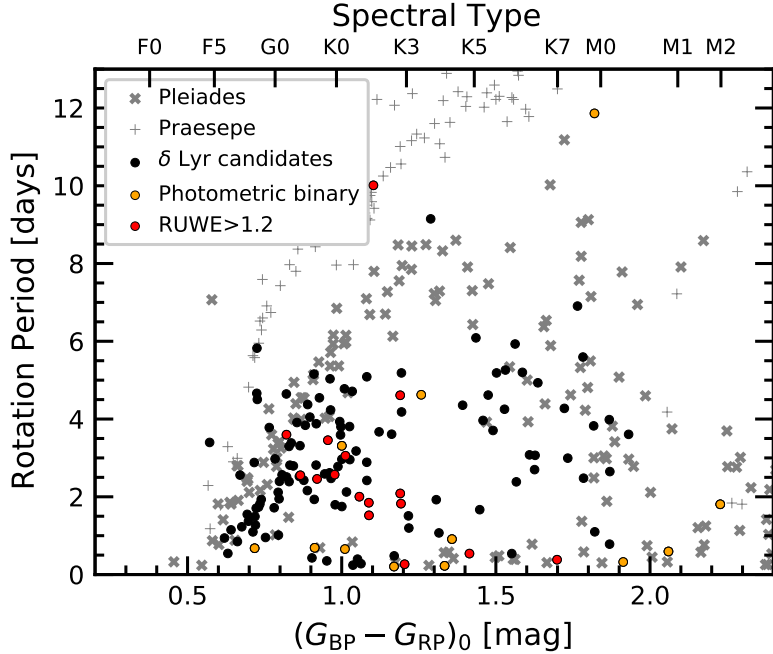


Figure 7. Binarity indicators for rotators in δ Lyr cluster. Data are as in the lower panel of Figure 2. Sources with $\text{RUWE} > 1.2$ appear in red; these include astrometric binaries as well as sources poorly fit by a single-star PSF. Photometric binaries (>0.3 mag above an empirical isochrone; 20% of stars) are orange. Over $0.6 < (G_{\text{BP}} - G_{\text{RP}})_0 < 1.5$, the detected rotation periods in binaries tend to fall below the slow sequence.

D. TRANSIT AND STELLAR VARIABILITY MODEL

We fitted the Kepler long cadence time series with a model that simultaneously included the planetary transit and the stellar variability. The stellar variability was modelled with the `RotationTerm` Gaussian Process kernel in `exoplanet` (Foreman-Mackey et al. 2020). This kernel assumes that the variability is generated by a mixture of two damped simple harmonic oscillators with characteristic frequencies set by $1/P_{\text{rot}}$ and its first harmonic. We additionally included a jitter term to inflate the flux uncertainties in a manner that accounted for otherwise unmodelled excess white noise, and let the eccentricity float. For the limb-darkening, we assumed a quadratic law, and sampled using the uninformative prior suggested by Kipping (2013).

Our model therefore included 10 free parameters for the transit ($\{P, t_0, R_p/R_\star, b, u_1, u_2, R_\star, \log g, e, \omega\}$), 2 free parameters for the light curve normalization and uncertainty calibration ($\{\langle f \rangle, \sigma_f\}$), and 5 hyperparameters for the GP ($\{\sigma_{\text{rot}}, P_{\text{rot}}, Q_0, dQ, f\}$). We also considered including an additive `SHOTerm` kernel to account for stochastic noise, but found that this did not significantly affect the results, and so opted for the simpler GP kernel. We fitted the models using `PyMC3` (Salvatier et al. 2016; Theano Development Team 2016), and accounted for the finite integration time of each exposure in the numerical integration when evaluating the model light curve (see Kipping 2010). We assumed a Gaussian likelihood, and after initializing each model with the parameters of the maximum *a posteriori* model, we sampled using `PyMC3`'s gradient-based No-U-Turn Sampler (Hoffman & Gelman 2014) in these bases indicated in Table 2. We used \hat{R} as our convergence diagnostic (Gelman & Rubin 1992).

Figure 3 shows the resulting model in orange (top) and purple (bottom). While the fit appears reasonably good, an asymmetry is present during the transit: the measured flux is systematically high during the first half, and low in the second half. To determine whether this effect was caused by our stellar variability model, we explored an alternative approach in which we isolated each transit window and locally fitted out polynomial trends, and then binned all the observed transits; the asymmetry was still present, at a comparable amplitude.

As a means of exploring the robustness of the asymmetry, Figures 8, 9, and 10 show the Kepler data binned in three ways: over quarters, years, and local slope quartiles. Over quarters (Figure 8), Quarter 6 shows the strongest asymmetry out of any quarter: a deviation of about 3 ppt from expectation. Quarter 7 shows an anomaly at roughly the same transit phase. Year 2 correspondingly shows the strongest anomaly out of any year in Figure 9; the asymmetry is visually apparent however in each of Years 2, 3, and 4. Binned by local

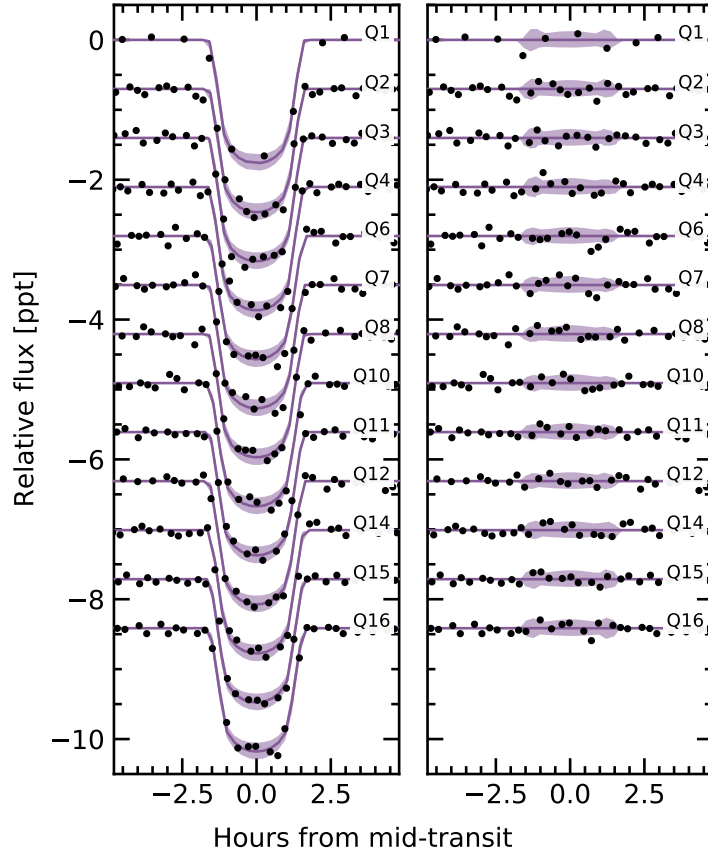


Figure 8. Transit model residuals through time (binned by Kepler quarter). *Left:* Phase-folded transit of Kepler 1627b, with stellar variability removed. Black points are binned to 20 minute intervals. The 2σ model uncertainties and the maximum *a posteriori* model are shown as the faint purple band, and the dark purple line. *Right:* As on the left, with the transit removed. Quarters 6 and 7 show a consistent deviation in the second half of the transit.

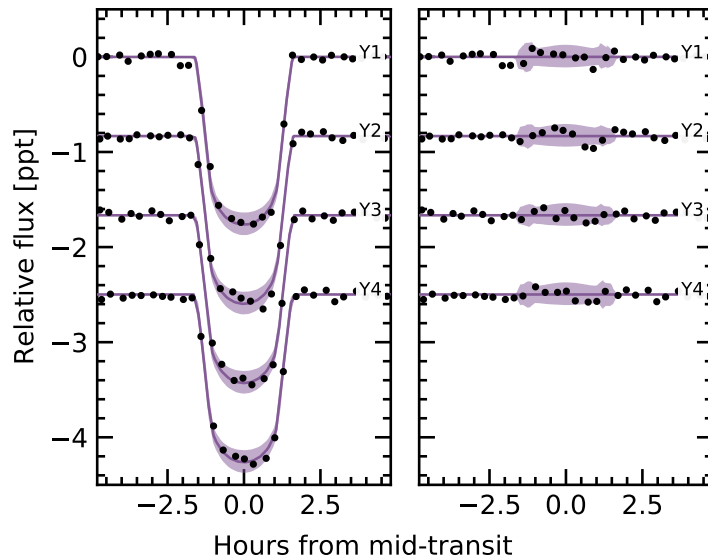


Figure 9. Transit model residuals through time (binned by year of observation). *Left:* Phase-folded transit of Kepler 1627b, with stellar variability removed. Points and models are as in Figure 8. *Right:* As on the left, with the transit removed.

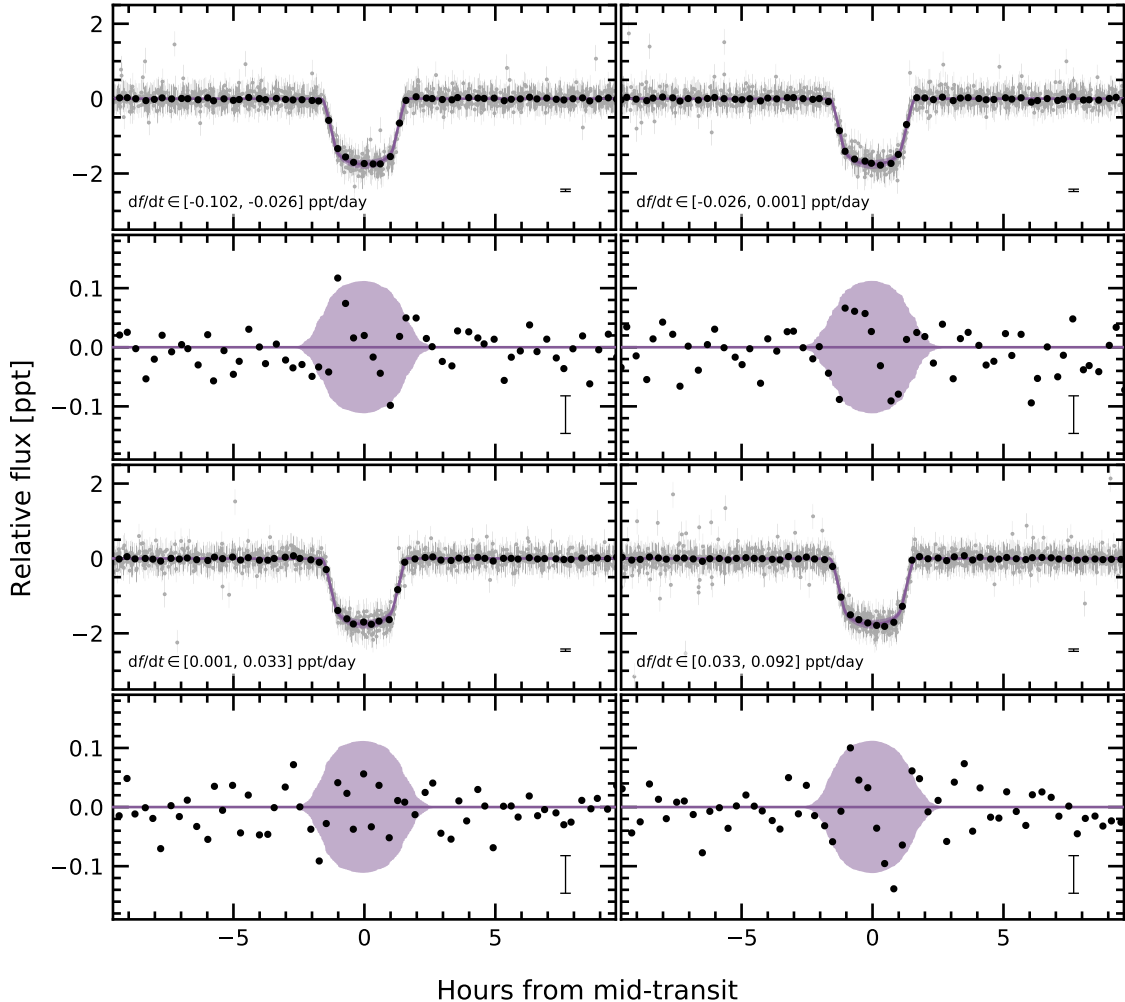


Figure 10. Transit models and residuals, binned by local slope of the raw light curve. Local linear slopes are measured over each transit window (144 transits total). Four outlier transits were removed, leaving 140 transits. These were then divided into quartiles, so that each panel shows 35 transits binned together. The exact light curve slopes are listed in the lower left panels. Representative uncertainties for the black points (binned at 20 minute intervals) are shown in the lower right of each panel. A similar transit asymmetry to that shown in Figure 3 seems to be present in three of the four bins.

slope quartiles (Figure 10), the asymmetry is visually present in three of the four quartiles: the only bin for which it appears to not be present is $df/dt \in [0.001, 0.033]\text{ ppt day}^{-1}$.

We considered four possible interpretations of the transit asymmetry: gravity darkening, transit timing variations, spot-crossing events, and a persistent asymmetric dusty outflow.

Gravity darkening is based on the premise that the rapidly rotating star is oblate, and brighter near the poles than the equator (*e.g.*, [Masuda 2015](#)). The fractional transit shape change due to gravity darkening is on the order of $(P_{\text{break}}/P_{\text{rot}})^2$, for P_{break} the break-up rotation period, and P_{rot} the rotation period. Using the parameters from Table 2, this yields an expected 0.14% distortion of the ≈ 1.8 ppt transit depth: *i.e.*, an absolute deviation of ≈ 2.5 ppm. The observed residual has a semi-amplitude of ≈ 50 ppm. Since the expected signal is smaller than the observed anomaly by over an order of magnitude, gravity darkening seems to be an unlikely explanation.

The scenario of transit timing variations (TTVs) producing the asymmetry seems unlikely because our analysis showed that transit timing variations in Kepler 1627 have amplitudes smaller than ≈ 10 minutes (see Figure 4). This is consistent with previous results from [Holczer et al. \(2016\)](#). Moreover, the transit timing variations we do observe are correlated with the local light curve slope, which on average increases as much as it decreases. From our analysis, the mean TTV and its standard deviation are 0.00 ± 12.05 minutes;

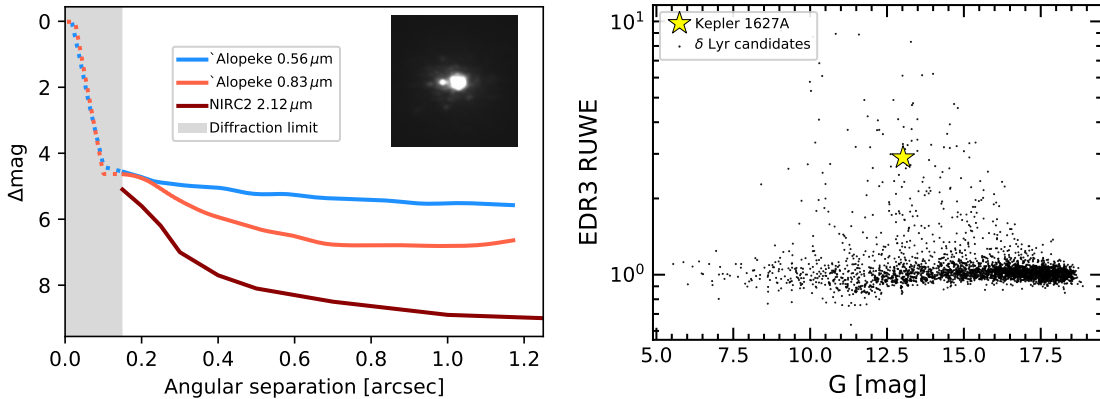


Figure 11. Kepler 1627 is a binary. *Left:* High-resolution imaging from Gemini-North/‘Alopeke and Keck/NIRC2 shows an \approx M2.5V companion at $\rho \approx 0.^{\prime\prime}16$, which corresponds to a projected separation of 53 ± 4 AU. The inset shows a cutout of the stacked NIRC2 image (North is up, East is left, scale is set by the separation of the binary). The lines show $5-\sigma$ contrast limits for the ‘Alopeke filters, and $6-\sigma$ contrast limits for NIRC2. Inside the diffraction limit (estimated as the gray band), the detection limits are less reliable. *Left:* Gaia EDR3 renormalized unit weight error (RUWE) point estimates for Kepler 1627A and other members of the δ Lyr cluster reported by Kounkel & Covey (2019). Since other members of the cluster with similar brightnesses have comparable degrees of photometric variability, the high RUWE suggests that Kepler 1627 is a binary.

similarly the mean local slope and its standard deviation are $0.49 \pm 44.49 \text{ ppt day}^{-1}$. There is therefore no expectation for TTVs to produce the asymmetry. A separate line of argument comes from Figure 10. If the local slope were essential to producing the transit asymmetry, we would expect that in the largest $\text{d}f/\text{d}t$ bin, $\text{d}f/\text{d}t \in [0.033, 0.092] \text{ ppt day}^{-1}$, the sign of the asymmetry would reverse. We do not see evidence for that being the case.

The third and related possibility is that of starspot crossings. Young stars have higher spot-covering fractions than old stars (e.g., Morris 2020). Young solar-type stars may also host dark starspots at high stellar latitudes (e.g., EK Dra; Strassmeier 2009), though interferometric imaging of spotted giant stars has shown different starspot latitude distributions than those inferred from Doppler imaging (Roettenbacher et al. 2017). Regardless, for any spot-crossing anomalies to add coherently over the 144 Kepler transits, it seems likely that we would need either for spots to be persistent at a particular latitude (and for the planetary orbit to be quite misaligned), or for a “stroboscopic” longitudinal phasing (e.g., Dai et al. 2018). For our system, $P_{\text{orb}}/P_{\text{rot}} \approx 2.76$, which means that every 4 transits and 11 stellar rotations, the planet crosses over roughly the same stellar longitude, which might enable the necessary phasing if the spot-groups are large and long-lived. Unfortunately, the S/N per Kepler transit is ≈ 8 , which renders individual spot-crossing events unresolved. This explanation seems marginally plausible, because the expected spot-crossing anomaly amplitudes (≈ 100 ppm) resemble the observed amplitude of the asymmetry (≈ 50 ppm). We ultimately disfavor it though, because *a*) it seems implausible that the starspot crossings could add coherently, and *b*) there is no reason to expect starspot crossing events to last exactly half the transit duration.

A persistent feature of the planet itself might therefore be needed to explain the transit asymmetry. An asymmetric outflow from the planet’s atmosphere could at least geometrically meet the requirements (e.g., McCann et al. 2019). To explain the asymmetric transit, a small, dense component would lead the planet, and a long, more rarefied (and variable) component would trail it. This might also explain the slight flux decrement visible for ~ 1 hour pre-ingress (Figure 3). The amplitude of the asymmetry is roughly in line with theoretical expectations for dusty outflows (Wang & Dai 2019), and based on the planet’s size, its mass is likely in a regime where such outflows are possible. Out of the four explanations discussed, this one currently seems the most plausible. By composition, the expectation would be that the envelope is mostly hydrogen and helium gas, with a dust or haze component providing the broadband opacity in the Kepler bandpass. A natural path toward confirming or refuting this idea would be to observe additional transits of the planet in hydrogen absorption, metastable helium absorption, or across a broad wavelength range in the near-infrared.

E. COMPANION STAR AND FALSE POSITIVE ASSESSMENT

We first noted the presence of a close neighbor on 2015 July 22 when we acquired adaptive optics imaging of Kepler 1627 using the NIRC2 imager on Keck-II. We used the narrow camera ($\text{FOV} = 10.2''$) to obtain 8 images in the K' filter ($\lambda = 2.12 \mu\text{m}$) with a total exposure time of 160 s. We analyzed these data following Kraus et al. (2016), beginning by applying standard reduction steps (dark-subtraction, flat-fielding, linearization, and bad pixel correction). We then used PSF-fitting to measure the separation, position angle, and contrast of the candidate companion, identifying the best-fitting empirical PSF template from among the near-contemporaneous observations of single stars in the same filter. Finally, we used the optical distortion solution of Yelda et al. (2010) to convert pixel-space relative positions to on-sky relative astrometry. The mean values inferred from the 8 images are reported in Table 1.

We also estimated detection limits following Kraus et al. (2016), analyzing the residuals after subtracting the empirical PSF templates, as well as the residuals after subtracting an azimuthally smoothed PSF profile. Within each residual image, the flux was measured through 40 mas apertures centered on every pixel, and then the noise as a function of radius was estimated from the RMS within concentric rings. Finally, the detection limits were estimated from the strehl-weighted sum of the detection significances in the image stack, and we adopted the $+6\sigma$ threshold as the detection limit for ruling out additional companions. We find contrast limits of $\Delta m_{K'} = 5.1$ mag at $\rho = 150$ mas, $\Delta m_{K'} = 7.0$ mag at $\rho = 300$ mas, and $\Delta m_{K'} = 9.0$ mag at $\rho > 1000$ mas. Given the distance ($d = 330$ pc) and age ($\tau \sim 40$ Myr), the models of Chabrier et al. (2000) imply corresponding physical limits on tertiary companions of $M_{\text{ter}} < 50M_{\text{Jup}}$ at $\rho = 50$ AU, $M_{\text{ter}} < 20M_{\text{Jup}}$ at $\rho = 100$ AU, and $M_{\text{ter}} < 10M_{\text{Jup}}$ at $\rho = 330$ AU.

We also observed Kepler 1627 on Gemini-North using the ‘Alopeke speckle imager on 2021 June 24. ‘Alopeke is a dual-channel speckle interferometer that uses narrow-band filters centered at $0.83 \mu\text{m}$ and $0.56 \mu\text{m}$. We acquired three sets of 1000×60 msec exposures during good seeing ($0.45''$), and used the autocorrelation function of these images to reconstruct a single image and 5σ detection limits (see Howell et al. 2011). This procedure yielded a detection of the companion in the $0.83 \mu\text{m}$ notch filter, but not the $0.56 \mu\text{m}$ filter. The measured projected separation and magnitude difference are given in Table 1.

Figure 11 summarizes the results of the high-resolution imaging. The Gaia EDR3 parallax for the primary implies a projected separation of 53 ± 4 AU, assuming the companion is bound. Although the companion is unresolved in the Gaia source catalog (there are no comoving, codistant candidate companions brighter than $G < 20.5$ mag within $\rho < 120''$), its existence was also suggested by the primary star’s large RUWE, relative to other members of the δ Lyr cluster. Based on the apparent separation, the binary orbital period is of order hundreds of years. The large RUWE is therefore more likely to be caused by a PSF-mismatch skewing the Gaia centroiding during successive scans, rather than true astrometric motion. Regardless, given the large observed RUWE of the primary, and the low geometric probability that a companion imaged at $\rho \approx 0.''16$ is a chance line-of-sight companion, we proceed under the assumption that the companion is bound, and that Kepler 1627 is a binary. Given the distance and age, the models of Baraffe et al. (2015) imply a companion mass of $M_{\text{B}} \approx 0.33M_{\odot}$ and companion temperature of $T_{\text{eff,B}} \approx 3450$ K. The corresponding spectral type is roughly M2.5V (Pecaut & Mamajek 2013).

Could the companion be creating a false positive signal? The companion star contributes $\approx 1\%$ of the total flux observed in the Kepler aperture. The observed transit has a depth of 0.18%. An 18% deep eclipse of the secondary star would therefore be needed to produce a signal with the appropriate depth. The shape of the observed signal requires the impact parameter to be below 0.74 (Table 2); the body transiting the secondary would therefore need to be non-grazing with $R_3/R_2 \approx 0.42$. Assuming a $\approx 0.46R_{\odot}$ radius of the imaged secondary from the Baraffe et al. (2015) models, this would imply a tertiary stellar radius of $\approx 0.2R_{\odot}$. This yields a contradiction: this scenario would require an ingress and egress phase that each span $\approx 40\%$ of the transit duration (≈ 65 minutes). The actual measured ingress and egress duration is ≈ 15 minutes), $4.4\times$ shorter. The combination of the companion’s brightness, transit depth, and ingress duration therefore rule out the scenario that it could explain the transit signal. Two other arguments presented in the main text – the inferred stellar density, and the TTV-local slope correlation – confirm this point.

F. SPECTROSCOPIC TRANSIT ANALYSIS

We monitored Kepler 1627 with Keck/HIRES before, during, and after transit on the night of 2021 Aug 7. We used the iodine cell for wavelength calibration⁸, extracted the 1-D spectra using the standard California Planet Survey pipeline (Howard et al. 2010), and measured the velocities by cross-correlating against a tem-

⁸ We considered a line-profile based analysis in the regions without iodine, but the line profile stability of HIRES precludes such an approach.

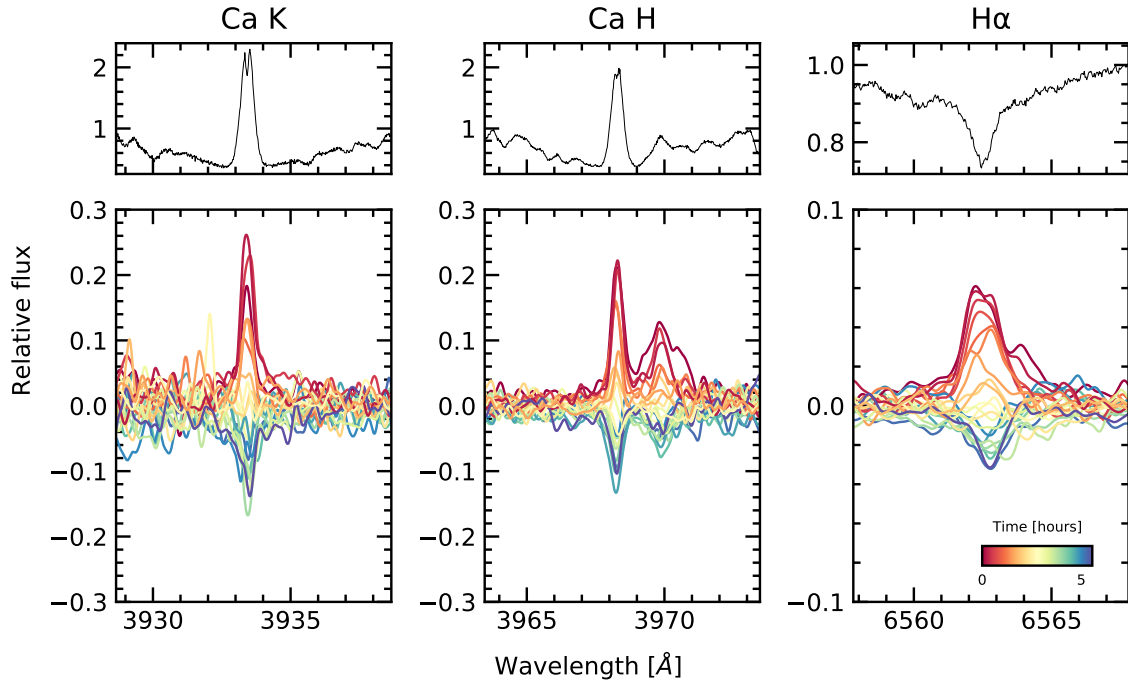


Figure 12. Spectroscopic activity indicators during the transit of 2021 Aug 7. The *top panels* show the median line profiles Ca K, Ca H, and H α line profiles from the HIRES spectra. The *lower panels* show the differences of each individual spectrum relative to the median spectrum. The bump in the red wing of Ca H is He. The spectra in the lower panels are smoothed for visualization purposes.

plate found via spectral classification with SpecMatch-Emp (Yee et al. 2017). The airmass ranged between 1.1 and 2.2 from the start through the end of observations; the seeing ranged from 1. $''$ 1 at the beginning to 1. $''$ 5 at the end. We also simultaneously observed across *griz* bands using MuSCAT3 at Faulkes Telescope North on Maui, HI.

The lower panels in Figure 4 show the results. The MuSCAT3 photometry shows the expected starspot trend, along with the transit and what is likely a chromatic starspot crossing event at JD – 2459433 = 0.955. The radial velocities decrease by 800 m s $^{-1}$ over the six hour window. A \approx 50 m s $^{-1}$ increase in RV is seen shortly after the expected ingress time.

Overall, we expect the dominant trends in both the photometry and radial velocities to be caused by starspots on the stellar photosphere rotating into and out of view. The plasma in the leading and receding limbs of the stellar disk has an apparent line-of-sight velocity of ± 20 km s $^{-1}$. Over 10% of a rotation cycle ($P_{\text{rot}} = 2.6$ days), spots near these limbs come into and out of view, modulate the stellar velocity profile, and can thereby produce the overall 800 m s $^{-1}$ trend. The Ca HK and H α emission profiles support this interpretation; Figure 12 shows that each line gradually decreases in intensity over the course of the six hour sequence. The overall RVs are also heavily correlated against the S-indices derived from the Ca HK lines.

The expectation however is for the starspot-induced signals to be smooth, at worst with contributions at 0.5 P_{rot} or 0.25 P_{rot} (Klein & Donati 2020). We therefore fitted the RVs using the Hirano et al. (2010, 2011) models for the Rossiter-McLaughlin (RM) effect, and allowed for an optional linear and quadratic trend in time to fit the 800 m s $^{-1}$ spot-induced trend. We followed the methodology developed by Stefansson et al. (2020). We allowed the sky-projected obliquity, the projected stellar equatorial velocity, and the Gaussian dispersion of the spectral lines to vary, and fixed the limb-darkening using the *V*-band tabulation from Claret & Bloemen (2011). We assumed a prior on $v \sin i$ and a/R_{\star} from Table 1, and also allowed for a white-noise jitter term to be added in quadrature to the measurement uncertainties.

The quadratic model with the RM effect is shown in Figure 4; the jitter term is incorporated in the model uncertainties, but not the plotted measurement uncertainties. The plotted measurement uncertainties are the internal uncertainties on the RVs (≈ 15 m s $^{-1}$), and are dominated by the $v \sin i$ broadening. However, between exposures, the RVs show significant additional scatter that is not captured by the slow quadratic trend. The

white-noise jitter for this particular model is $\sigma_{\text{RV}} = 50^{+11}_{-8} \text{ m s}^{-1}$, which is larger than the expected RM anomaly of $\Delta v_{\text{RM}} \approx f_{\text{LD}} \cdot \delta \cdot v \sin i \cdot \sqrt{1 - b^2} \approx 20 \text{ m s}^{-1}$.

The presence of this additional scatter prevents a clear detection of the RM effect. The reason can be understood via model comparison. If we compare the model with a quadratic trend and the RM effect (Figure 4) against a model with a linear trend and the RM effect, or even a model with no RM effect at all, then the respective Bayesian Information Criterion (BIC) values are as follows.

$$\begin{aligned} \text{BIC} &= 251.7 \quad (\text{Quadratic + RM}) \\ \text{BIC} &= 257.7 \quad (\text{Linear + RM}) \\ \text{BIC} &= 247.1 \quad (\text{Only Quadratic}). \end{aligned} \quad (\text{F1})$$

There is therefore no evidence to prefer the model with the RM effect against a model that only accounts for the stellar variability. The “only quadratic” model does particularly well because it can inflate the jitter term to account for scatter during the transit (even if the scatter contains astrophysics!), and it has fewer free parameters. However, we cannot justify a physical prior on the jitter term, because we do not understand the origin of the exposure-to-exposure scatter. As noted above, the velocity deviations from starspots are expected to have contributions at the stellar rotation frequency, or harmonics thereof. This jitter is present on the exposure timescale (15 minutes), which is only 0.4% of the stellar rotation period; it is not obvious that starspots would be the culprit.

The amplitude of both the spot-induced trend and the jitter are larger than recent comparable measurements in systems such as AU Mic (Palle et al. 2020), DS Tuc (Montet et al. 2020; Zhou et al. 2020) and TOI 942 (Wirth et al. 2021). One possible explanation for the jitter is that it is astrophysical in origin, and that it is caused by some novel process operating on the surface of Kepler 1627A. Another possibility is that our RV analysis underestimates the measurement uncertainties; the S/N per resolution element for each of our spectra was moderated by the observing requirements to 70 to 80, and the rapid rotation of the star could affect accuracy of the uncertainties from the velocity extraction. Observations at higher precision are necessary to distinguish these two possibilities, and remain worthwhile as a means toward clarifying the orbital geometry of Kepler 1627Ab.

G. FLARE ANALYSIS

In addition to the 3.9 years of long cadence data, short cadence (1-minute) Kepler observations were acquired over 97.7 days during Quarter 15. The short cadence light curve shows a higher rate of flaring than visible in the long cadence data (Figure 13). We analyzed the short cadence light curve and its flares according to the following procedure.

1. Fit the starspot-induced variability using a Gaussian Process with a SHOTerm kernel (see Section D), a white-noise jitter term, and the mean flux.
2. Select points more than twice the median absolute deviation from the residual, and exclude them from the light curve (these points include the flares). Repeat Step 1.
3. Using the residual from Step 2, identify all flares, requiring them to be at least 20 cadences apart, at least 7 median absolute deviations above the median baseline, and lasting at least 2 cadences in duration. Build the mask spanning these times, from 5 minutes before each flare begins to 2.5 minutes after the final flare cadence. Repeat Step 1 a final time.

The final step of flare identification and fitting was performed using `altaipony` (Davenport 2016; Ilin et al. 2021). The analytic flare model is from Davenport et al. (2014) and it parametrizes the flare with a start time, an exponential lag time, and an amplitude.

There were $N_f = 24$ flares that exceeded 0.5% in relative flux during the short cadence observations. These 24 flares spanned a total of 6.5 hours (~ 15 minutes per flare). Inspecting the data, we noticed a coincidence in the flare arrival times. The coincidence is that despite the low flare duty cycle, one orbital period after the brightest flare, a second flare followed. This and a similar event are shown in Figure 13. The timing error is good to a $\approx 0.2\%$ difference from the orbital period, which given the duty cycle seems *a priori* unlikely. If we consider flares falling within 2% of the planet’s orbital period after a previous flare, then 4 of the 24 flare events have candidate “successors”.

As with any coincidence, if one does not have a firm prediction, it is difficult to assess whether a surprise is statistically significant. Since our surprise was specifically at the inter-arrival time of certain flares coinciding

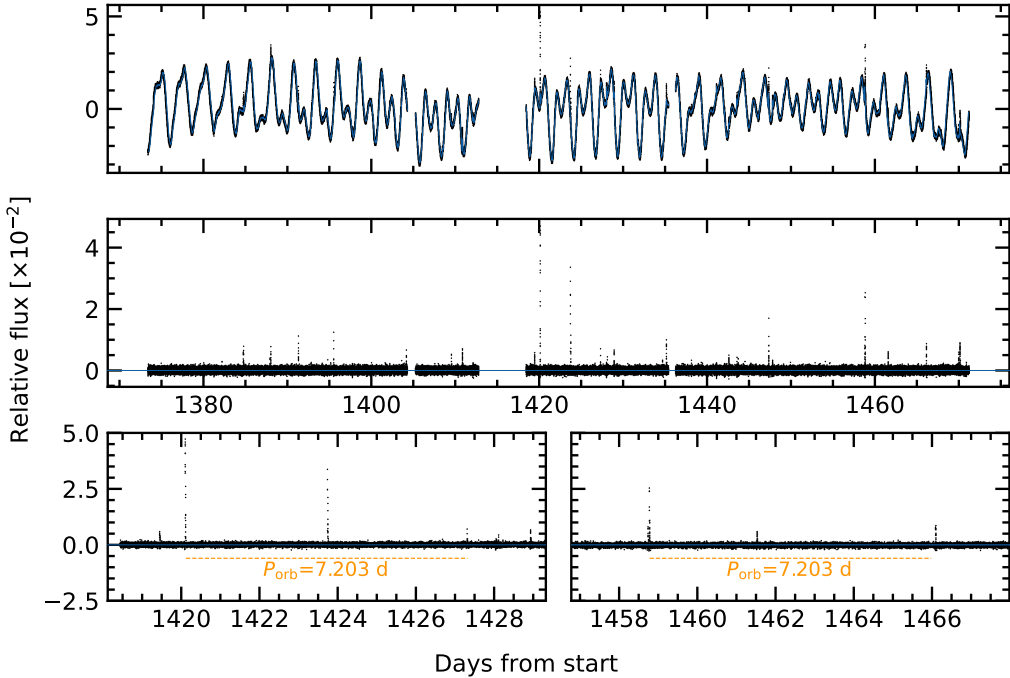


Figure 13. Flares in Kepler 1627. *Top:* The full short cadence Kepler dataset, acquired at 1-minute sampling (black points) is shown with a stellar variability model (blue line). *Middle:* Residual after subtracting the stellar variability model. Flares appear as spikes. *Bottom:* Zooms of the brightest, and third-brightest flares. A timing coincidence – that both flares have “successors” approximately one orbital period after the initial event – is emphasized.

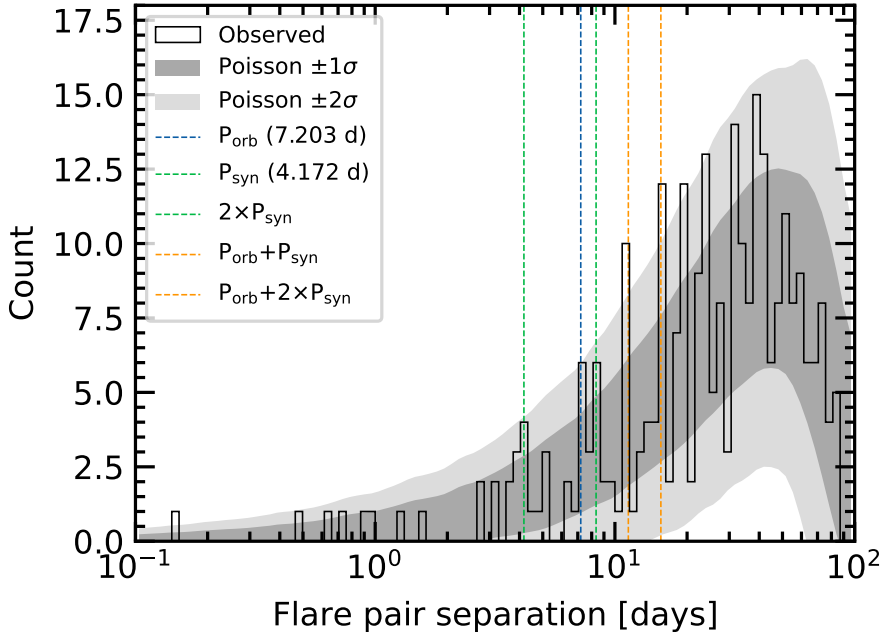


Figure 14. Statistics of inter-flare arrival times. 24 flares were recorded with amplitudes exceeding 0.5% over the 97.7 days of short cadence observations. The histogram of the time intervals between every possible pair of flares is shown in black. Some plausibly important timescales for star-planet interactions, namely the planetary orbital period and synodic period (the orbital period as seen from the rotating stellar frame) are shown along with their linear combinations. Monte Carlo draws from a Poisson distribution are shown with the gray bands. While peaks in the observed distribution do coincide with some of the “special periods”, the statistical evidence for a non-Poissonian process driving the flares does not reach the 5σ threshold.

with special time intervals, we performed the following analysis. First, we considered all unordered pairs of flares. For N flares there are $\binom{N}{2}$ such pairs (for our case, 276 pairs). We then compared the distribution of the pair separations against that of a Poisson distribution. Specifically, we drew $N_f = 24$ samples from a Poisson distribution with $\lambda = \Delta t / N_f$, for $\Delta t = 97.7$ days the total duration of the observations, and repeated the draw 10^3 times with unique random seeds.

Figure 14 shows the results. The vertical lines in the figure show the planetary orbital period, the synodic period $P_{\text{syn}} = (P_{\text{rot}}^{-1} - P_{\text{orb}}^{-1})^{-1}$, and linear combinations thereof. The tidal period (half the synodic period) is not shown. The bins are logarithmically spaced to give 100 bins between the minimum and maximum ordinate values. The gray bands express the range of values observed from the Poissonian draws. While it does seem like an odd coincidence for peaks in the observed flare arrival time distribution to coincide with the locations of these “special intervals”, the statistical evidence for a non-Poissonian process driving the flares does not seem especially overwhelming. More quantitatively, the peaks observed at the orbital and synodic periods are within the $\pm 2\sigma$ range of a Poissonian process, and those at $P_{\text{orb}} + P_{\text{syn}}$ and $P_{\text{orb}} + 2P_{\text{syn}}$ are only slightly above this range. With that said, future analyses of these data by investigators with more knowledge of this topic could very well yield more quantitative insights. Such analyses should keep in mind an important caveat: the amplitude distribution of M-dwarf flares extends up to many times the quiescent flux (see Figure 7 of Günther et al. 2020). A flare on Kepler 1627B producing double its quiescent white-light flux would yield a $\approx 1\%$ apparent amplitude. Such flares could represent a significant fraction of those in the Kepler observations.